# Tubule jamming in the developing kidney creates cyclical mechanical stresses instructive to *in vitro* nephron formation

John M. Viola[1,2]*, Jiageng Liu[1,2]*, Louis S. Prahl[1]*, Aria Huang[1,2], Trevor J. Chan[1,2], Gabriela Hayward-Lara[3], Catherine M. Porter[1,2], Chenjun Shi[4], Jitao Zhang[4], Alex J. Hughes[1-3,5-7,†]

[1]Department of Bioengineering, University of Pennsylvania, Philadelphia, 19104, PA, USA.
[2]Bioengineering Graduate Group, University of Pennsylvania, Philadelphia, 19104, PA, USA.
[3]Cell and Molecular Biology Graduate Group, University of Pennsylvania, Philadelphia, 19104, PA, USA.
[4]Department of Biomedical Engineering, Wayne State University, Detroit, 48201, MI, USA.
[5]Department of Cell and Developmental Biology, University of Pennsylvania, Philadelphia, 19104, PA, USA.
[6]Center for Soft and Living Matter, University of Pennsylvania, Philadelphia, 19104, PA, USA.
[7]Institute for Regenerative Medicine, University of Pennsylvania, Philadelphia, 19104, PA, USA.

*These authors contributed equally

[†]Corresponding author. Email: ajhughes@seas.upenn.edu

## Abstract

The kidney develops through elaboration of ureteric bud tubules (the future urinary collecting ducts), stroma, and nephron progenitors in the cap mesenchyme that surround each tubule tip as they branch. Dynamic interactions between these tissues coordinate a balance between ureteric bud (UB) tip branching and nephron formation that sets nephron numbers for life, which impacts the likelihood of adult disease. How then is this balance achieved? Here we study the geometric and mechanical consequences of tubule tip crowding at the embryonic kidney surface and its effect on nephron formation. We find that kidney surface curvature reduces and tubule 'tip domains' pack more closely over developmental time. These together create a semi-crystalline geometry of tips at the kidney surface and a rigidity transition to more solid-like tissue properties at later developmental stages. New tips overcome mechanical resistance as they branch, expand, and displace close-packed neighbors, after which residual mechanical stress dissipates. This correlates with a changing nephrogenesis rate over the tip 'life-cycle'. To draw a causal link between the two, we mimic a mechanical transient in human iPSC-derived nephron progenitor organoids and find increased cell commitment to early nephron aggregates. The data suggest that temporal waves of mechanical stress within nephron progenitor populations could constitute a pace-maker that synchronizes nephron formation and UB tubule duplication after E15. Ongoing efforts to understand the spatial and temporal regulation of nephron induction will clarify variation in nephron endowment between kidneys and advance engineered kidney tissues for regenerative medicine.

## Introduction

Tissue-building processes during embryonic kidney development set the number of nephrons and urinary collecting tubules in the adult organ, since no further nephrons are added after postnatal day 4 in mice and 36 weeks of gestation in humans[1]. The number of nephrons formed in development varies substantially between kidneys and individuals, impacting the likelihood of adult kidney disease[2–4]. However, there is limited knowledge on the local and global processes that set nephron numbers. Given that all nephrons are induced by nearby ureteric bud (UB) tubules, this is at least partially explained by a lack of temporal and spatial

consistency in kidney branching morphogenesis. Namely, branching of the UB is asynchronous and asymmetric (meaning that the number of descendants of tubules at the same branch generation are different)[5,6]. Further, while biochemical cues passed between the tips of the UB tree and nephron stem cells in the surrounding cap mesenchyme are well characterized[7–11], the time and place at which any given nephron forms cannot be predicted. Gaining a predictive understanding of nephrogenesis is crucial to engineering approaches to kidney replacement technologies and in vitro tissue models, since these must achieve high nephron density and structural connectivity with UB tubules to function[12].

During development, the ureteric bud branches into kidney mesenchyme and the tubule tips subsequently present Wnt ligands to dynamic clusters of cap mesenchyme cells that proliferate and serve as nephron progenitors[9,13]. Meanwhile signaling pathways including BMP/pSMAD and Wnt/β-catenin induce cap mesenchyme cells to periodically condense and undergo mesenchymal-to-epithelial transition at elbow regions beneath UB tips[7,14]. Nephrons first form as spherical pre-tubular aggregates and later develop into renal vesicles, comma-shaped and S-shaped bodies, simultaneously invading and forming patent lumens with the adjacent UB tip and setting the proximodistal axis of the nephron[15,16].

These tissue-building processes are concentrated at the surface of the kidney, with all UB tips present at the surface throughout development rather than distributed in deeper tissue layers[17]. In recent work, we found that the position of UB tips at the kidney surface are partially predictable through a physical model of tip repulsion and crowding[18]. Preliminary analysis of tip positions at the surface revealed different crystal-like packing geometries that were at least locally ordered. These observations suggested an analogy to 2D curved crystals of repulsive particles[19–23]. Such crystals have several fascinating physical properties that could impact the developmental trajectory of the kidney by setting limits on tip and therefore nephron number for a given organ surface area, and by changing the physical microenvironment of tips over their elongation and branching cycles.

The nephron progenitor microenvironment is highly dynamic, unlike many adult stem cell niches in which cells reside in a geometrically fixed microenvironment (e.g. gut crypts, the basal layer of the skin). This is due to extensive cell motility, proliferation, and division of cap mesenchyme populations among daughter UB tubules after each bifurcation event[17,24,25]. The size of cap mesenchyme populations and the proximity of cells to signaling cues produced by the UB and stroma is in constant flux[26]. Yet the number of nephrons doubles at the same rate as tips do, since the average number of nephrons per tip is fixed at ~2 over E15-P2[17]. Nephron progenitors could be induced stochastically at exactly the appropriate rate to achieve this[25], but what sets this rate is unknown. One hypothesis is that a pace-making mechanism operates at the collective cell scale that tunes the induction rate by sensing geometry or mechanics of the cap mesenchyme niche.

Here we combine the theory of curved crystals, rigidity in close-packed systems, and force inference with analysis of mouse embryonic kidneys and human iPSC-derived kidney organoids to study the interplay between geometry, mechanics, and differentiation in the cap mesenchyme. Our data reveal temporal cycles of mechanical stress within this nephrogenic niche. These cycles may constitute a pace-maker that sets an appropriate frequency of nephron induction by synchronizing nephron formation with the ureteric bud tip life-cycle. Synthetic intervention in this developmental ‘module’ has significant potential for *in vitro* kidney engineering efforts relevant to regenerative medicine.

## Results

### Ureteric bud tubule geometry is partially determined by kidney curvature

During branching morphogenesis, UB tubules duplicate just beneath the kidney surface. Each tip is surrounded by a swarm of 'cap' mesenchyme cells that serve as nephron progenitors, with each cap repelling each other[24,27,28], creating dense arrays of tips separated by thin sheets of stroma (**Fig. 1A, Movie S1**). We previously noted an analogy for close packing of caps in the physics of repulsive or elastic particles at surfaces[18]. The geometry and mechanics of packing in such systems are affected by particle density and surface curvature[23,29,30]. We thus began by considering the contribution of kidney curvature to the geometric microenvironment of individual UB epithelial tips. Repulsive particles pack most efficiently on flat surfaces in a hexagonal close-packed (triangular lattice) fashion where each particle has six neighbors (i.e. the coordination number $z = 6$) (**Fig. 1B**). However, wrapping a triangular lattice onto a surface with Gaussian curvature creates an energetic cost that favors the emergence of topological defects called disclinations, in which particles have greater or fewer than six neighbors. Secondly, for curved crystals that are sufficiently large, isolated dislocations are less favorable and are replaced by pairs, clusters, or chains ('scars') having 'excess' dislocations (**Note S1**)[19,20,22]. We therefore wondered if UB tip positions adhere to the same topological requirements that set defect number and organization in curved crystals.

We began by annotating UB tip positions on kidneys over embryonic days E14-E17. This allowed us to extract the predicted lattice boundaries of each tip 'domain' (all UB epithelium, cap mesenchyme, and stroma closer to a given tip than to a neighboring one) using a Voronoi tessellation approach. We then separately reconstructed their surfaces from 3D confocal image stacks to compute their curvature maps (**Fig. S1**). Tip positions and Voronoi diagrams describing tip domains are shown in **Fig. 1C-F**. We also colored tip domains according to the number of neighbors they contact (the coordination number $z$), which is related to their 'topological charge' $s = 6 - z$ (**Fig. 1G**). Tip coordination numbers varied between 4 and 8, and tip patterns qualitatively transitioned from a disordered state at E14-E15 to more visually apparent local order at E16-E17 (see also [18]). Voronoi analysis successfully predicted the position and boundaries of tip domains (**Fig. 1G**), suggesting that their size and shape are restricted by the presence of neighboring domains. A similar correspondence has been noted in 2D foams and confluent cell monolayers[31,32]. The median coordination number of tips was $z = 6$, with a bias toward lower coordination number at earlier developmental times. This is consistent with tip patterns adopting energetically favorable pentagon disclinations (i.e. tips with $z = 5$ neighbors instead of 6) in younger kidneys with higher curvature (**Fig. 1H,I**). At later times, the coordination number distribution narrowed and approached a mean of 6, consistent with predictions for particle packings on flat surfaces (**Fig. 1I**). The theory of curved crystals suggests that the amount of bias toward pentagon dislocations will increase linearly with curvature (**Note S2**). Indeed, we find substantial agreement with the prediction of a bias toward pentagonal tip domains for younger kidneys with greater curvature per confocal region of interest (**Fig. 1J**). While variation in tip domain size and shape appears to contribute to the majority of excess dislocations in the kidney case, we also see evidence of grain boundary scars and clusters of defects of alternating charge (**Fig. 1C-F**). These data show that tip packing geometry at the kidney surface is partially determined by topological limitations imposed by kidney curvature.

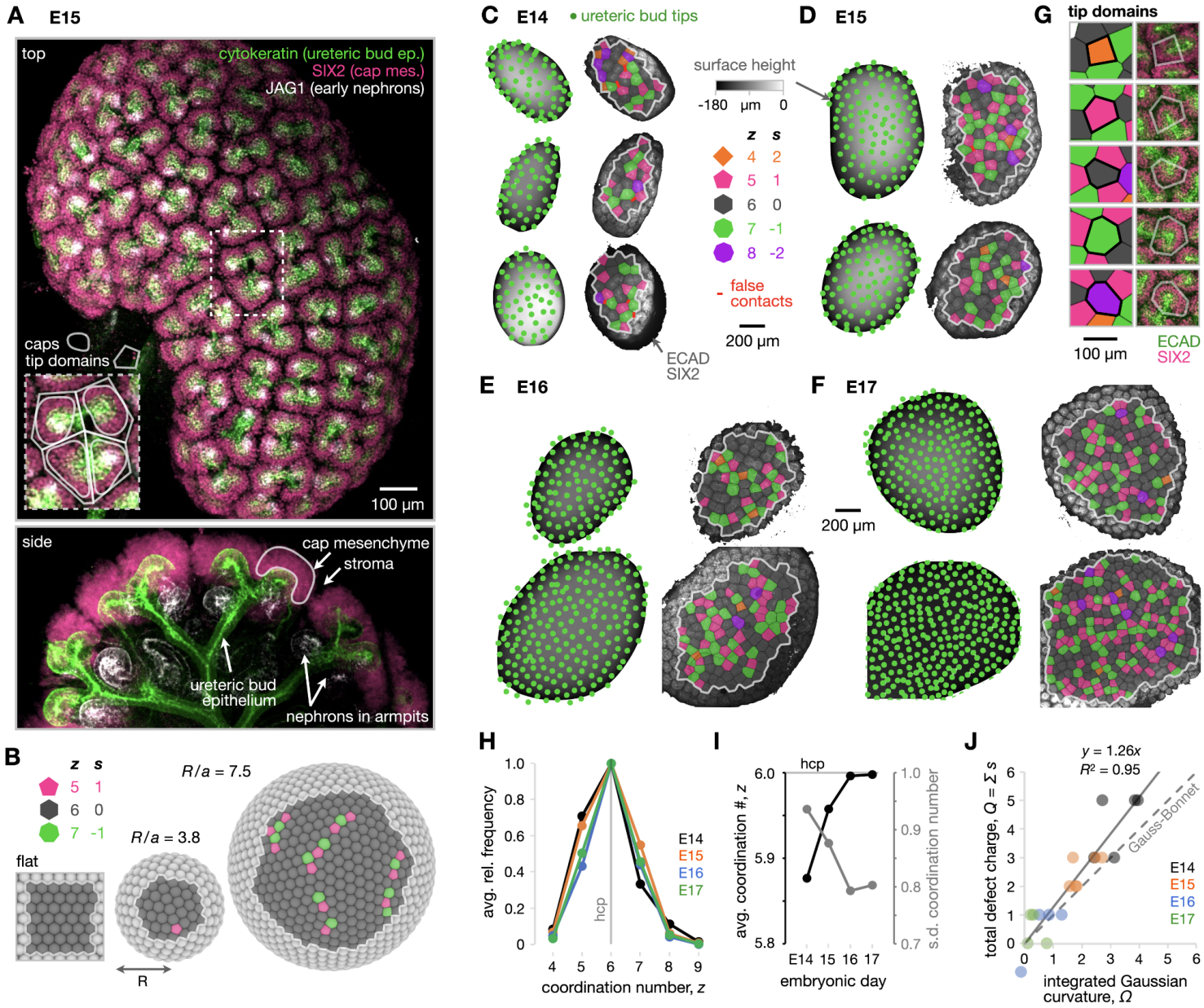


**Fig. 1: Kidney curvature imposes topological requirements on geometry of close-packed ureteric bud tubules.** (**A**) Confocal fluorescence maximum projection (top) and xz plane for embryonic day (E)15 mouse kidney. Branching cytokeratin+ UB tubule tips are surrounded by SIX2+ nephron progenitors in the cap mesenchyme. Caps are separated by a thin layer of stroma (unlabeled). JAG1+ early nephrons form at 'armpits' beneath tubule tips. (**B**) Schematic of repulsive particle (radius *a*) packing at the surface of a sphere (radius *R*), showing pentagonal and heptagonal topological defects amongst an otherwise hexagonal packing. Defects form pairs, clusters, or chains for $R/a > 5$. (**C-F**) *Left*, height maps of representative kidney surfaces over E14-E17 overlayed with UB tip positions. *Right*, micrographs of combined ECAD and SIX2 immunofluorescence overlayed with Voronoi diagrams tracing 'tip domains'. Voronoi cells are colored by coordination number (# neighbors). (**G**) Example Voronoi cells and corresponding tip domain boundaries. (**H**) Frequency plot of tip domain coordination number (for (**H**)-(**J**), $n$ = 5, 6, 4, 4 kidneys and 162, 353, 535, and 892 tip domains in E14, E15, E16, and E17 categories, respectively). (**I**) Average and standard deviation (s.d.) of coordination number distributions. (**J**) Sum of defect charge (i.e. net decrease in coordination number from $z = 6$) plotted against integrated Gaussian curvature for patches of kidney surface (units of disclinations).

**Crowding of ureteric bud tip domains creates crystal-like packing patterns and a mechanical rigidity transition**

Beyond the contribution of curvature to the geometric microenvironment of UB tip domains, we sought to understand the impact of crowding among neighboring mesenchyme caps, each bordered by intervening layers of stroma. During early branching morphogenesis, caps and stroma are both fluid-like on a developmental timescale[24,33] (**Note S3**). However, the stroma thins over E14-E18, causing caps to pack closer together, conform in shape because of the confinement imposed by neighboring caps, and locally align with each other[18]. Similar geometric features are observed in confined packings of soft elastic spheres[29] or closely packed droplets in dense two-phase emulsions such as foams[34–36]. Since the degree of crowding can create abrupt changes in the geometric and mechanical properties of these systems, we wondered if similar effects could occur during cap packing. One such property is a so-called density-dependent rigidity (jamming) transition that occurs when droplets crowd together beyond a critical volume fraction $\phi_c$ and transition from zero to some finite yield stress (i.e. from fluid-like to solid-like behavior)[37,38]. For kidney caps, we determined $\phi$ on a 2D basis as the ratio of cap area to total area. This area fraction $\phi$ exceeded those for 2D body-centered (square) packing of circles and for random close packing (which defines $\phi_c$[37,39,40]), even approaching that for 2D hexagonal close packing (hcp) after ~E15 (**Fig. 2A**). This predicts a jamming transition, such that the 'nephrogenic zone' as a whole is predicted to be solid-like and therefore capable of imposing mechanical stress on newly formed caps during tip duplication after ~E15.

Although $\phi$ predicts density-dependent jamming of caps, the underlying theory reduces potentially important parameters to a passive interfacial tension[37,41]. These parameters include collective cell elasticity and active contractility (embryonic kidney cortex explants shrink in the hours after cutting[18]), and extra contributions to interfacial tension at cap-stroma boundaries (tissue layers are adhered through cell-cell junctions and/or cell-extracellular matrix interfaces). We therefore made some further predictions using a density-independent rigidity theory created for the high packing fraction regime that does consider these parameters. This theory considers jamming in 2D cell monolayers using a cell vertex model[42–44]. We instead applied it at the higher-level organizational scale of tip domains, since the underlying mechanical energy terms are equally applicable to tip domains as to cells (see **Methods**). The vertex model as applied to cells predicts a transition to rigidity when the median of a geometric parameter of cell boundaries called the shape index $p$ (**Fig. 2B**) drops below a critical shape index $p^*$ [42,43]. When $\bar{p} > p^*$, there is no energy barrier to transitions between different packing configurations, conferring fluid-like mechanics. However, when $\bar{p} < p^*$ the configuration of cells has both bulk and shear stiffnesses, conferring solid-like mechanics[44].

One explanation for a fluid-like to solid-like transition upon reducing median shape index comes from rigidity theory, in which a mechanical assembly is rigid when the number of degrees of freedom of nodes matches the number of constraints[30,45]. This predicts rigidity for a polygonal tiling of cells when $\bar{p} < p^* = 3.81$ (above $\bar{z} = 5$)[42], and when $\bar{p} < p^* = 3.91$ (above $\bar{z} = 4.5$) for tip domains (**Fig. 2C**, **Note S4**). We measured the shape index of tip domains over E14-E17, finding that the median shape index significantly decreased with developmental time, dropping below 3.91 after E15 (**Fig. 2D**). Despite a relatively small effect size, the change in shape index here is in a similar range to that previously associated with a rigidity transition in airway epithelial cells[43]. This result suggested that the mechanical microenvironment of tips may become stiffer and less viscous after E15, consistent with the time at which crystal-like locally ordered regions began to appear in **Fig. 1**.

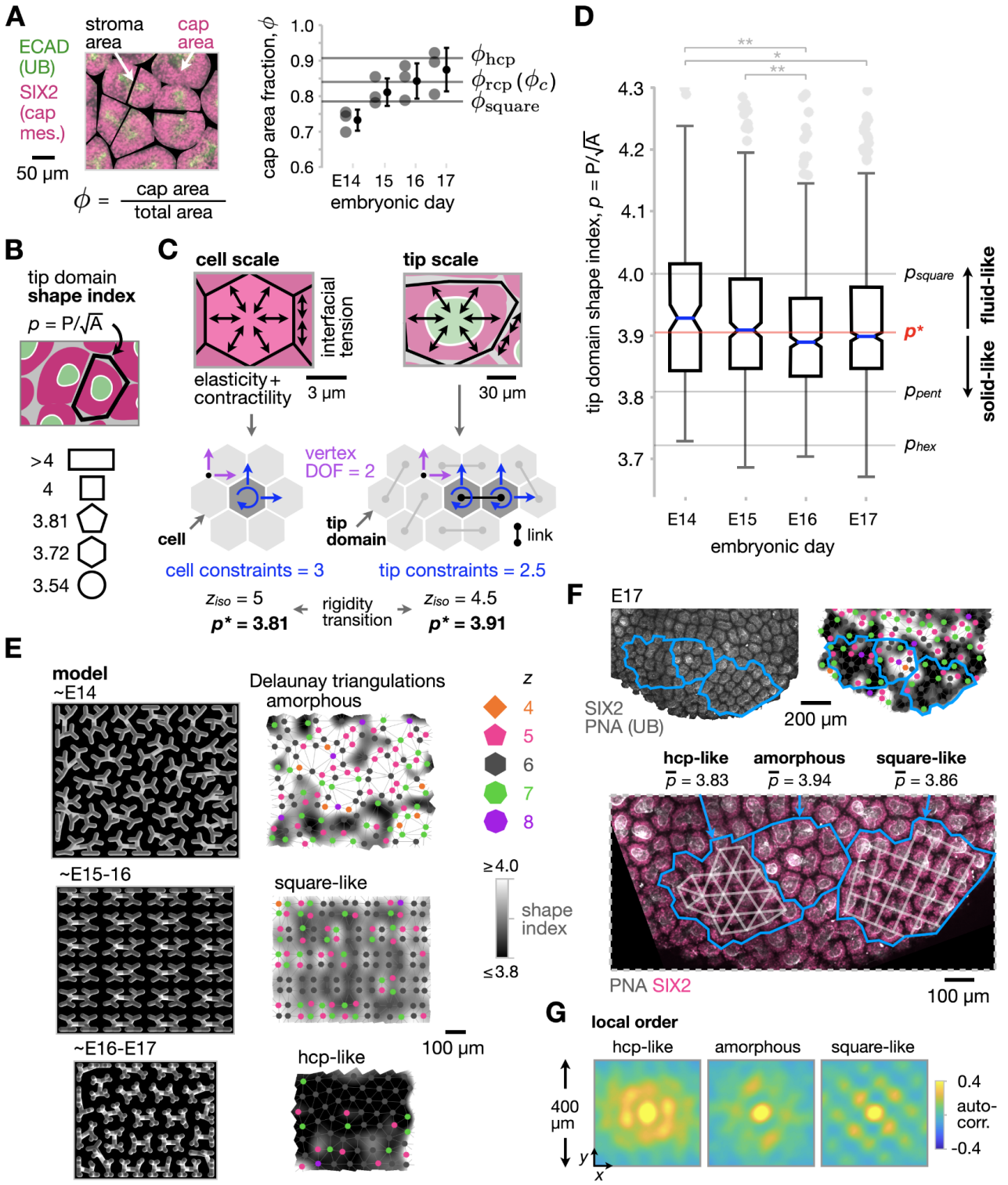


**Fig. 2: Close packing of ureteric bud tips predicts a transition to rigidity and emergence of semi-crystallinity over developmental time.** (**A**) *Left*, Segmented confocal micrograph indicating the area fraction $\phi$ of cap mesenchyme. *Right*, Plot of $\phi$ over developmental time relative to 2D square packing, random close packing (rcp), and hexagonal close packing (hcp) of circles (mean ± S.D., $n$ = 3 kidneys per embryonic day, average over > 12 tip domains per kidney). (**B**) Definition of shape index of tip domains $p$ from Voronoi cell perimeter (P) and area (A). (**C**) Isostaticity (degree of freedom) analysis to define rigidity threshold in terms of critical average coordination number $z_{iso}$ and critical shape index $p^*$ for the cell vertex model (*left*), and adapted to coupled tip domains (*right*), DOF = degrees of freedom. (**D**) Box plots of tip domain shape index distributions over time, relative to those for squares, pentagons (*pent*), and hexagons (*hex*), and to $p^*$ = 3.91 ($n$ = 5, 6, 4, 4 kidneys and 177, 391, 617, and 987 tip domains in E14-17 categories, respectively. One-way ANOVA, Tukey's test: *p < 0.05, **p < 0.01, ***p < 0.001). (**E**) *Left column*, Representative physical model output for

tubule packing regimes characteristic of the indicated developmental ranges, previously reported in [18]. *Right column*, overlays of Delauney triangulations indicating coordination number of tip domains on spatial heatmaps of shape index, showing reducing shape index as tip patterns transition from amorphous to square-like to hcp-like regimes. (**F**) Representative case study of amorphous and crystalline phases of tip domain packing at E17. *Top*, Confocal micrograph of tip domains and shape index heatmap. Example regions of different packing regimes are outlined in blue. *Bottom*, Inset of these regions showing lattice lines and decreasing median shape index $\bar{p}$ from amorphous to square-like to hcp-like packing. (**G**) Study of positional order within regions in (**F**) by spatial autocorrelation.

To draw a connection between shape index and our previous geometric model of tubule family packing, we produced heat maps of tip domain shape index for three characteristic regimes of tip packing that we identified in previous work[18]. These three regimes, which at the tip domain level can be qualitatively referred to as amorphous, square-like, and hcp-like respectively, mirror the reduction in tip domain shape index from E14-E17 (**Fig. 2E**). In reality, tip packing does not perfectly adhere to any one regime at a snapshot in time (**Fig. 2F**). This could be caused by disruption of packed regions due to asynchronous tip duplication that would displace neighbors (**Movie S2A**) and create heterogeneity (polydispersity) in the relative size and shape of tip domains (quantified later in **Fig. 4**). This means that our previous model predicts the stage at which a given packing phase has the potential to exist, but a mixture of phases arises in practice. For example, at E17 we observe regions that exhibit amorphous, square-like, or hcp-like packing geometry. These regions persist spatially for 2-3 tip spacings in *xy*, as revealed by spatial autocorrelation analysis showing four-fold and six-fold rotational symmetry for square-like and hcp-like regions respectively (**Fig. 2G**). Overall, these data show that tip domain packing at the kidney surface is semi-crystalline with an increased prevalence of square packed and hcp regions at later developmental times.

We next wondered if our predictions from rigidity theory and the increase in crystalline order of tip domains over time would correlate with tissue mechanical properties on the length-scale at which tip domains interact. We predicted that this would manifest both spatially and temporally - firstly that tip domains in regions of higher crystalline order (lower local average *p*) should show higher stiffness, and that the overall increase in tip domain crystallinity over time would also increase tissue stiffness. Taking advantage of the accessibility of tip domains at the kidney surface, we employed Brillouin microscopy and surface microindentation to quantify spatial and temporal changes in tissue mechanics, respectively.

We tackled the spatial aspect using confocal Brillouin microscopy[46,47], a label-free optical technique that has been previously used to quantify the embryonic tissue mechanics of the spinal cord, cornea, and fly ventral furrow during gastrulation[48–50]. Brillouin microscopy measures the frequency shift (i.e., Brillouin shift) between incident and scattered light caused by the interaction of incoming photons with inherent (spontaneous) acoustic waves in biological materials[51] (**Fig. 3A**). The Brillouin shift scales with the high-frequency longitudinal modulus, a uniaxial stress-to-strain ratio that is proportional to the more widely known quasi-static Young's modulus *E* ('stiffness') in cells and tissues over a physiological range relevant to embryonic development[47,52]. We acquired 2D Brillouin images of randomly chosen E17 tip domains at planes approximately bisecting tubule tips and surrounding mesenchyme (**Fig. 3A**). We found that the mean Brillouin shift in cap mesenchyme cells and the average shape index in a local neighborhood of ~3 tips were strongly correlated (**Fig 3B**); specifically that the longitudinal modulus of cap mesenchyme is significantly higher for tip domains predicted to reside in more closely packed and solid-like regions with crystalline order (**Fig. 2D-G**). Although accurately translating the high-frequency Brillouin modulus to the quasi-static Young's modulus requires careful calibration specific to a given sample, we can approximate the relative change in Young's modulus based on an empirical log-log linear relationship established using cells (Zhang et al, Small, 2020). For a Brillouin shift increase of ~0.1 GHz, the relative increase in Young's modulus is ~46%. These data show that the stiffness of nephrogenic niches varies substantially over the kidney surface and is significantly higher for tips in regions with closer-packed geometry.

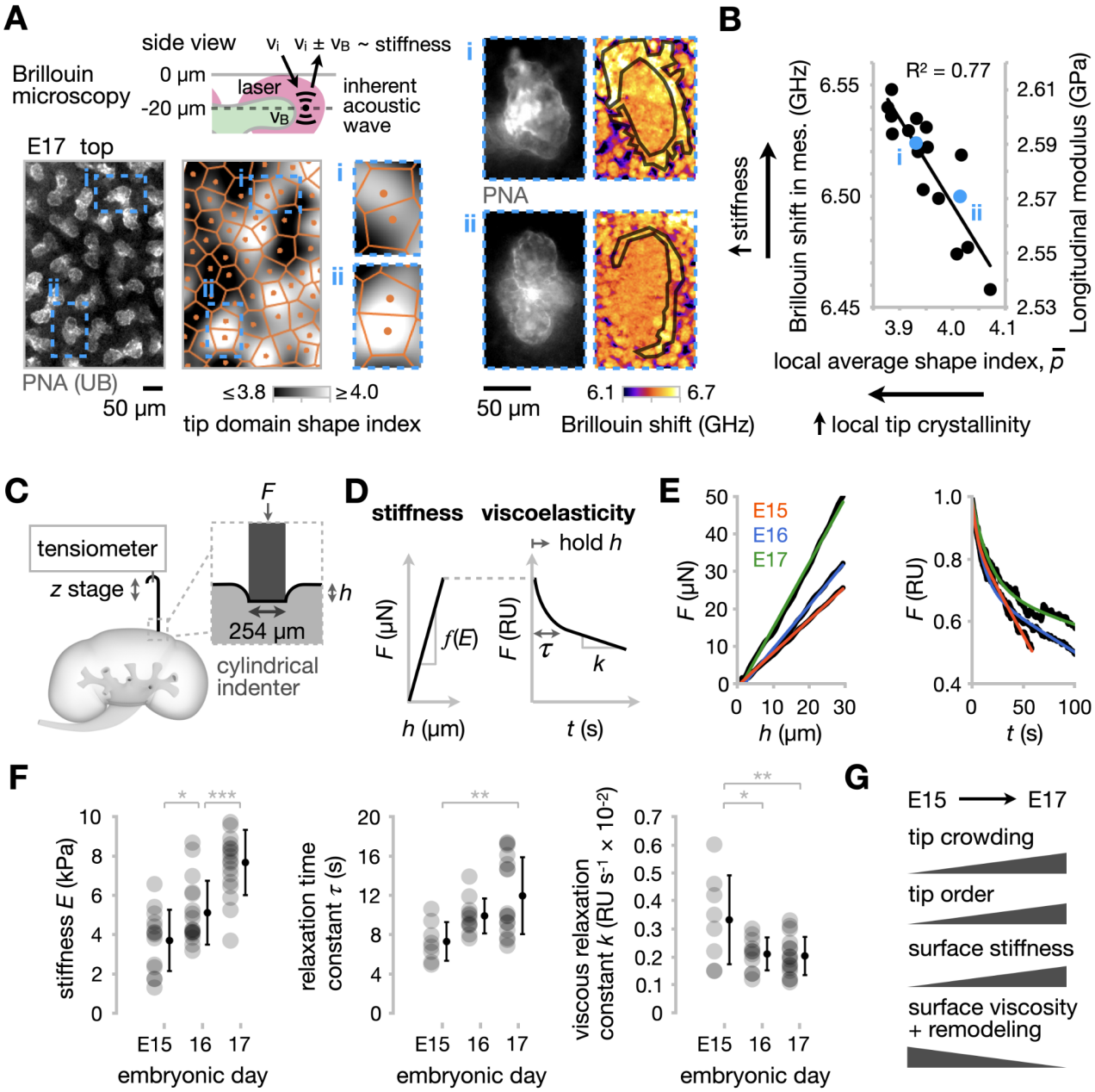


**Fig. 3: Crowding of ureteric bud tip domains stiffens the nephrogenic niche in close-packed regions and overall in developmental time.** (**A**) *Top*, Schematic of Brillouin microscopy, which quantifies an optical frequency shift that depends on tissue stiffness. *Bottom*, live confocal micrograph of PNA-labeled UB tips, Voronoi diagram of tip domains with heatmap of shape index, and zoomed insets of two example domains. *Right*, Insets of the two example domains with PNA fluorescence and Brillouin shift images. Cap mesenchyme cells local to tips are outlined. (**B**) Mean Brillouin shift and corresponding estimated longitudinal modulus in cap mesenchyme cells vs. average tip domain shape index in their local neighborhood of ~3 tips ($n$ = 17 tip domains across 4 E17 kidneys). (**C**) Schematic of surface microindentation using a cylindrical indenter that captures kidney viscoelastic properties on the length scale of ~3 tip domains for h ~ 30 µm. (**D**) Cartoon of typical data output and key parameters during indentation (*left*), and during subsequent recording of force at fixed final indentation depth (*right*). (**E**) Representative indentation force vs. indentation depth, and force relaxation curves for E15-E17 kidneys. (**F**) Stiffness, relaxation time $\tau$, and viscous relaxation constant $k$ plots over E15-E17 (mean ± S.D., $n$ > 14 kidneys per embryonic day for stiffness and > 8 for $\tau$ and $k$, one measurement per kidney. One-way ANOVA, Tukey's test: *p < 0.05, **p < 0.01, ***p < 0.001). (**G**) Summary of changes in UB tip geometry and kidney surface mechanics over E15-17.

We next sought to validate the time-dependent rigidity transition predicted in **Fig. 2D** using surface microindentation to quantify elastic modulus (stiffness) and viscoelasticity over E15-E17 using a 254 μm cylindrical indenter (equivalent to the width of ~3 tip domains, **Fig. 3C**, see **Methods**)[53]. We measured the applied force recorded during indentation of the kidney surface by ~30 μm, and paused indentation to capture the time dependence of force during subsequent tissue relaxation (**Fig. 3D**). These measurements revealed a significant increase in kidney surface stiffness local to tip domains over E15-17 (**Fig. 3E,F**). Secondly, they showed an increase in the time-scale of force relaxation over E15-E17, perhaps due to a slowing in passive remodeling of cell collectives and extracellular matrix[53]. Thirdly, the measurements showed a decrease in viscous relaxation over E15-E17, perhaps caused by slowing of active tissue remodeling. Together, these data reveal marked increases in stiffness and decreases in passive and active tissue remodeling over E15-E17, the same time period over which our tip domain shape index analysis predicted a fluid-like to solid-like transition in tissue rigidity (**Fig. 2D**, **Fig. 3G**).

An increase in kidney surface stiffness and reduction in viscosity would increase the mechanical resistance to new tip domains forming, expanding, and displacing close-packed neighbors, creating residual stress (**Movie S2B**). This would imply that tip domains see cyclical swings in their mechanical microenvironment on a similar timescale to tip duplication events. The local packing state may even influence the balance of tip duplication and nephrogenesis events, either because of geometric changes in morphogen and growth-factor presentation to nephron progenitors, or because of mechanical influences on cell signaling. Mechanical modulation of progenitor differentiation can occur via intersection with Wnt/β-catenin signaling, for example in mesoderm specification of hESCs[54] and in morphogenesis of the avian feather primordium[55]. Mechanical modulation can also occur via intersection with BMP/pSMAD signaling, for example in translating anisotropic stress in the condensing digit mesenchyme into expression of digit organizing center genes[56]. In the kidney cap mesenchyme, both of these potentially mechanosensitive Wnt/β-catenin and BMP/pSMAD signaling axes (along with YAP[57]) are required for nephrogenesis (see **Note S5** for detail). However, the potential influence of a mechanical context in tip domains that fluctuates on the timescale of nephrogenesis has not been determined either *in vivo* or using stem cell models.

**Nephrogenesis rate varies over tip domain life-cycle**

If periodic swings in the geometric or mechanical microenvironment of tip domains affect nephrogenesis, we would expect to see periodic changes in nephrogenesis rate over the life-cycle of tip domains. However, it is not currently possible to live-image tip geometry and nephron formation in kidney explants while retaining their *in vivo* 3D architecture[58], so we instead attempted to extract correlative information from fixed explants. We focused on E17 kidneys, reasoning that periodic increases in local mechanical stress due to tip duplication would be amplified because of their higher surface stiffness and lower viscosity relative to earlier stages. Nephrons can be scored from immunofluorescence stacks by combining annotations of Six2+ spheroids beneath UB tips (capturing pre-tubular aggregate and renal vesicle stages) with annotations of sites where connecting tubules from more mature nephrons connect to tips (capturing comma shaped body, S-shaped body, and later stages), **Fig. 4A**. First, we found a negative correlation between tip domain area and shape index, which appears to reflect the 'life-cycle' of tips. Specifically, recently divided tips have lower area and higher shape index, while older tips are larger with lower shape index (**Fig. 4B**). The inference of tip age is revealed when we overlay the number of nephrons associated with each tip, namely that nephron number increases as tips grow in area and become more circular. When tips divide, their nephrons are divided among daughter tips[17], and the cycle repeats (**Fig. 4C**). These data imply that the tip domain shape index can be used as a "pseudotime" dimension that corrects for the lack of synchronization of tip duplication events.

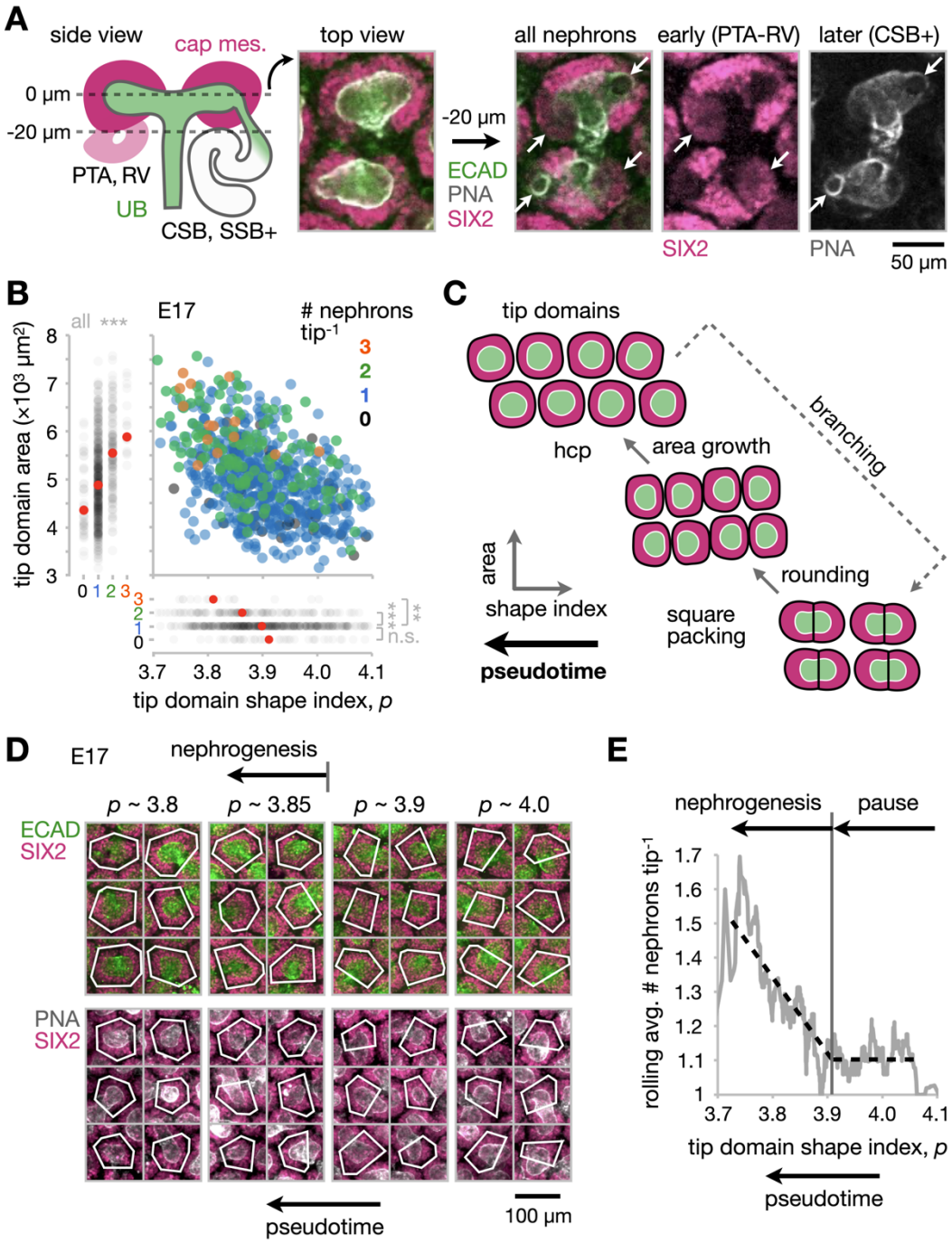


**Fig. 4: Nephrogenesis rate varies over a tip domain 'life-cycle' defined by shape index.** (**A**) *Left*, Cartoon showing side (*xz*) view of a pair of UB tips associated with early stage nephrons (PTA, pre-tubular aggregate; RV, renal vesicle) and later stage nephrons (CSB, comma shaped body; SSB, S-shaped body). *Right*, Confocal immunofluorescence micrographs at the mid-plane of UB tips and 20 µm deeper into an E17 kidney. All nephrons associated with each tip can be annotated either as SIX2⁺ spheroids for early nephrons or from the attachment points of their connecting tubules for later nephrons (white circles at tips in PNA channel), see arrows. (**B**) Plot of tip domain area against shape index, with nephron number per tip in the color dimension ($n$ = 694 tip domains across 4 E17 kidneys. One-way ANOVA, Tukey's test: *p < 0.05, **p < 0.01, ***p < 0.001). Each axis is also plotted individually vs. nephron number per tip. (**C**) Cartoon of UB tip life-cycle and definition of a pseudotime based on shape index of tip domains. N.B. asynchronous tip branching is not depicted for clarity. (**D**) Example confocal micrographs of tip domains over a range in shape index. (**E**) Running average of nephron number per tip against shape index (window width = 50 points).

In other words, tips in different locations can be aligned with respect to their progress through morphogenesis relative to their last duplication event (**Fig. 4D**). This enabled us to plot a rolling average of nephron number per tip against shape index. If nephron progenitors commit to early nephron aggregates stochastically[25] and at a fixed rate, we would not expect the nephrogenesis rate to depend on tip life-cycle. However, nephrogenesis appears to switch on as the shape index of tip domains drops below an intermediate value of $p \sim 3.91$ and the area of tip domains begins to increase (**Fig. 4E, Fig. S2**). This means that nephrogenesis pauses as new tips push outward against neighboring tip domains and begin to round up, and resumes as tip domains then grow in area.

**Newly branching tip domains experience mechanical stress that dissipates over their life-cycle**

After finding that nephrogenesis rate varies periodically with tip life-cycle, we wondered if mechanical stress local to tips would also depend on their life-cycle. To assess this, we drew on force inference methods developed from cell-scale vertex modeling to investigate mechanical heterogeneity in groups of UB tip domains[59–61]. Force inference has been successfully validated by laser ablation experiments across several model organisms, tissue types, and length-scales (from several-cell to highly multicellular tissues)[61]. We again reasoned that force inference could be extended to the analysis of tissue-level tip domain populations because both cells and tip domains can be described by equivalent mechanical energy terms in the underlying cell vertex model (**Fig. 5A, Methods**). We therefore performed force inference on Voronoi diagrams produced from E17 kidney surface projections to recover the inferred stress tensor, which yields major and minor principal stress axes and relative magnitudes that give relative isotropic and anisotropic (deviatoric) stresses (**Fig. 5B**). We plotted these components against the shape index of tip domains to show that as tips age relative to their last duplication event (i.e. as shape index decreases), they see a marginal increase in inferred isotropic stress, and a ~30% decrease in anisotropic stress (**Fig. 5C**). This indeed suggests a cyclical mechanical environment synchronized with the tip life-cycle, and in particular, that mechanical tension immediately precedes the nephrogenic phase and then falls most substantially as tip domain shape index drops below $p \sim 3.91$ (**Fig. 5C, Fig. 4E**).

We next sought to validate inferred stresses local to tip domains experimentally. We used laser microdissection of E17 kidney explants to create slot-like ablations spanning neighboring cap mesenchyme populations and orthogonal to the stromal boundary between pairs of UB tips (**Fig. 5D, Movie S3**). Laser ablation is thought to most closely reflect anisotropic stress at cutting sites[60], such that the rebound (opening) velocity of cut edges is proportional to local tension[61]. Ablation successfully induced rebound at cut sites (**Fig. 5D**), and cuts penetrated ~40 μm in depth, sufficient to sever the mesenchyme and stroma between tips over their full *z* extent (**Fig. 5E**). Validating the force inference data, the rebound velocity of cuts significantly increased with the average shape index of tip domains adjacent to each cut at E17 (**Fig. 5F, Fig. S3**). These data show that anisotropic stress local to the cap mesenchyme is highest for newly duplicated tips with higher shape index and lowest for older tips with lower shape index. This held for E17 kidneys but not for E15 kidneys prior to the rigidity transition (**Fig. 5F, Fig. S3**). This validates our earlier notion that in kidneys after the rigidity transition, newly formed tip domains are subjected to mechanical stress as they overcome physical resistance while branching and displacing close-packed neighbors. This tension then dissipates prior to the next duplication cycle (**Movie S2B**).

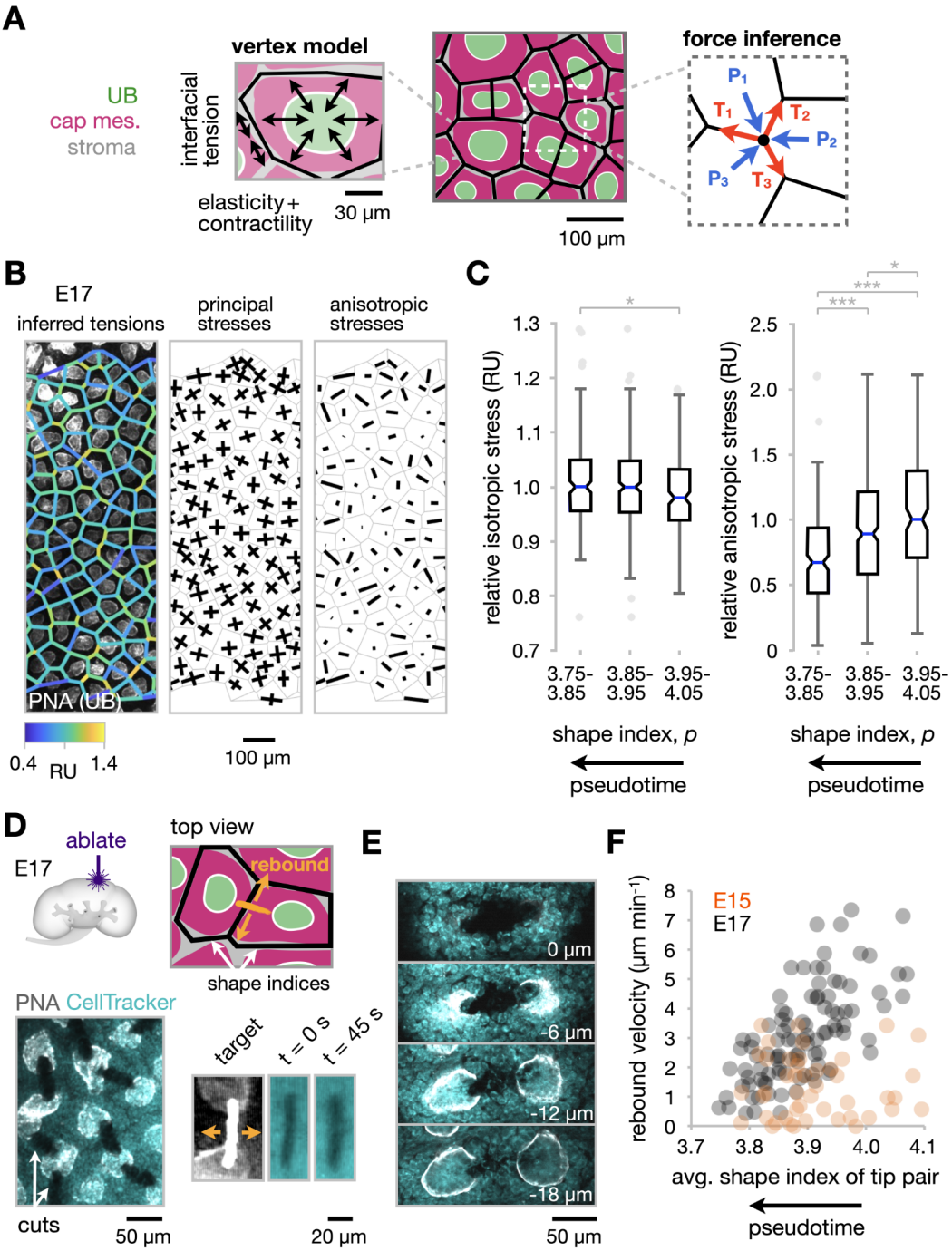


**Fig. 5: Newly established tip domains experience mechanical tension that decreases over each life-cycle.** (**A**) Schematic of inferred tension (T) and pressure (P) contributions to the force balance at an example node in a vertex model representation of tip domains. (**B**) Example force inference output from tip domain Voronoi geometry as a spatial map overlaid on confocal fluorescence micrograph of E17 kidney surface, along with relative principal and anisotropic stress vectors. (**C**) Box plots of isotropic and anisotropic stress for tip domains, relative to the median of the highest stress category in each plot ($n$ = 4 kidneys; 195, 319, and 164 tip domains in low, medium, and high shape index categories, respectively. One-way ANOVA, Tukey's test: *p < 0.05, **p < 0.01, ***p < 0.001). (**D**) *Top*, Schematic of laser microdissection ablation of cap mesenchyme and stroma orthogonal to boundaries between neighboring tip domains at E17. *Bottom*, Confocal micrograph showing example cuts after fixation, cut location prior to ablation by widefield fluorescence, and rebound of the cut in the 45 s after ablation. (**E**) Sequential z-slices in a confocal stack after fixation, showing penetration of a cut ~20 µm through the inter-tip region (cell integrity disrupted down to ~40 µm). (**F**) Plot of cut rebound velocity (change in cut width in 45 s) after ablation against the average shape index of the tip domains immediately adjacent to each cut ($n$ = 45 and 99 cuts pooled across 5 and 7 kidneys for E15 and E17 respectively).

**Mimicking transient cell-collective stress during tip domain branching increases nephrogenesis in kidney organoids**

After finding that nephrogenesis rate and tip domain mechanics vary periodically with tip life-cycle, we wondered if the two were causally connected. Although SIX2+ nephron progenitor induction via BMP/pSMAD and Wnt/β-catenin signaling axes is crucial for nephrogenesis, perturbations apparently unrelated to ligand secretion or spatial distribution also appear to affect it (see **Note S6** for detail). These include perturbations to kidney explant culture geometry and mechanics as well as to Rho/ROCK and non-muscle myosin II, which are important for cell tension and perception of the mechanical microenvironment[62,63]. Such disparate observations have not previously been interpreted in the light of mechanics of the nephrogenic niche, motivating further investigation.

Cytoskeletal tension and adhesion properties of cells often reflect biophysical properties of the tissue microenvironment, which can direct cell decision-making[54,64–67]. We wondered then if nephron progenitors mimic stiffness and tension changes in the tip domain microenvironment over the tip life-cycle. We began by analyzing differential gene expression in a recently published scRNA-seq analysis of nephron progenitor and committing cell sub-populations of E15.5 mouse kidneys[25]. Lawlor *et al.* confirmed differential expression of marker genes previously ascribed to these populations, including *Cited1* and *Six2* for nephron progenitors and *Wnt4, Pax8*, *Lhx1*, and *Jag1* for committing cells[25]. The top 10 Gene Ontology (GO) terms[68] associated with genes significantly upregulated in committing cells compared to progenitor cells included cell locomotion and cell migration, processes in which cell cytoskeleton, adhesion and mechanical properties change[69] (**Fig. S4A-B**). We therefore examined differential expression of genes combined from the cell migration GO term and pathways associated with cytoskeletal remodeling from the PathCards database[70]. We found significant increases in transcripts involved in cytoskeletal integrity and remodeling (nesprin-2, tropomyosin, Arp2/3), cell-cell junctions and adhesion (Claudin 5, *Podxl*, connexin 43, α-catenin), and cell-extracellular matrix adhesion (dystroglycan 1, collagen IV, laminin) in committing cells prior to significant differential E-cadherin expression (**Fig. 6A, Fig. S4C**). Preliminary observations by Brillouin microscopy also indicated that early nephrons are significantly stiffer than cap mesenchyme (**Fig. S5**). Together these data lend evidence of a change in cell mechanical state prior to and during early nephron epithelialization.

We next turned to a bottom-up approach using human iPSC-derived nephron progenitor organoids to assess the effects of mechanical microenvironment changes on nephron differentiation (**Fig. 6B**). When differentiated, these roughly mimic the progression in transcriptional states and marker expression profiles of mouse nephron progenitors *in vivo*, despite some species-specific differences[71–75]. To test perturbations to cell collective tension during nephron progenitor commitment, we first differentiated iPSCs through late primitive streak and posterior intermediate mesoderm (PIM) lineages to metanephric mesenchyme according to established protocols[76], confirming by qPCR (**Fig. S6**). We also validated that induced metanephric mesenchyme cells go on to form later nephron structures including ECAD+ tubules and cells expressing the proximal tubule marker LTL, the glomerular podocyte marker NPHS1, or the loop of Henle marker SLC12A1 ($Na^+/K^-/2Cl^-$ cotransporter) after 21 days in culture (**Fig. 6C**). Day 9 induced metanephric mesenchyme cells were dissociated and plated into low-attachment round-bottom plates where they formed spheroids that we assayed for early nephrogenesis (**Fig. 6B,F**). In similar assays, a CHIR pulse is typically applied after re-aggregation of cells to mimic Wnt9b-driven β-catenin signaling during nephron progenitor commitment *in vivo*[71,72,77,78]. We observed that CHIR also induced cell release from their substrate and compaction in day 9 iPSC-derived metanephric mesenchyme that appeared to occur due to collective cell contractility rather than motility (**Movie S4**). We took these cells as a model for Wnt9b-stimulated nephron progenitors in the high mechanical tension state shortly after tip duplication.

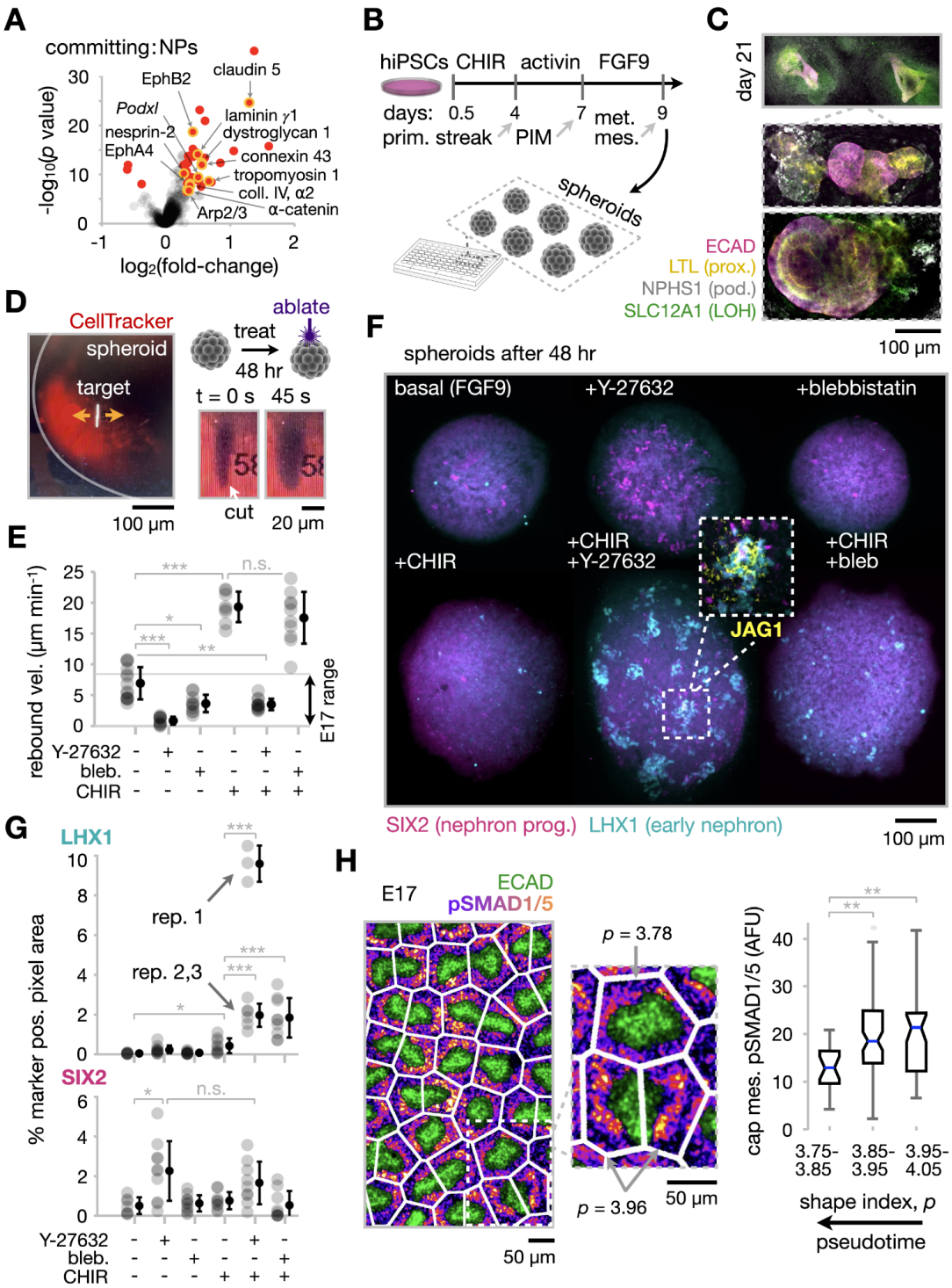


**Fig. 6: Mimicking decrease in mechanical tension increases nephron induction in human iPSC-derived kidney organoids.** (**A**) Volcano plot of differentially expressed cytoskeleton and cell migration genes for committing vs. progenitor populations from scRNA-seq data in ref. [25]. Red circles are significantly differentially expressed genes ($p < 0.01$ and fold-change > 1.2 or < 0.8). Coll., collagen. (**B**) Schematic of human iPSC differentiation to metanephric mesenchyme (met. mes.) and formation of spheroids for early nephron induction assays. Prim., primitive; PIM, posterior intermediate mesoderm. (**C**) Confocal immunofluorescence micrograph and insets of iPSC-derived metanephric mesenchyme after continued 2D differentiation in FGF9 basal media until day 21, with a CHIR pulse over days 9-11. Prox., proximal tubule; pod., podocyte; LOH, loop of Henle. (**D**) Schematic of laser microdissection ablation of metanephric mesenchyme spheroids. *Bottom right*, Widefield fluorescence micrographs of example cut location prior to ablation, and rebound of the cut in the 45 s after ablation. (**E**) Plot of cut rebound velocity (change in cut width in 45 s) after ablation for spheroids

treated with basal FGF9 media or basal media supplemented with CHIR, the ROCK inhibitor Y-27632, and/or the non-muscle myosin II inhibitor blebbistatin (mean ± S.D., $n > 7$ cuts across >3 spheroids per condition. One-way ANOVA, Tukey's test: *p < 0.05, **p < 0.01, ***p < 0.001). The range of rebound velocities reported for metanephric mesenchyme at the E17 mouse kidney surface in **Fig. 5F** is noted for comparison. (**F**) Representative confocal immunofluorescence projections of spheroids after 48 hr perturbations. *Inset,* Detail of Jag1 expression. (**G**) Plot of marker positive pixel areas as a % of projection area for markers of nephron progenitors (SIX2) and early nephron cells (LHX1) (mean ± S.D., $n > 6$ spheroids pooled across three replicates. One-way ANOVA, Tukey's test: *p < 0.05, **p < 0.01, ***p < 0.001). All conditions were comparable between replicates except for the +CHIR +Y27632 condition, where replicates (rep.) are reported separately. (**H**) *Left*, Confocal immunofluorescence of pSMAD1/5 in E17 kidney tip domains. *Right*, Box plot of mean cap mesenchyme pSMAD1/5 fluorescence of tip domains binned by their shape index ($n$ = 20, 76, and 37 tip domains pooled across 2 kidneys in low, medium, and high shape index categories, respectively. One-way ANOVA, Tukey's test: *p < 0.05, **p < 0.01, ***p < 0.001).

We then decided to mimic the reduction in tension that occurs over the tip life-cycle *in vivo* by adding the ROCK inhibitor Y-27632 or the non-muscle myosin II inhibitor blebbistatin to day 9 metanephric mesenchyme spheroids for 48 hr. These temporal parameters were optimized to capture early transitions of cells through the SIX2+ state and to accumulate differentiation events sparsely, enabling quantification. We first used laser microdissection to confirm that CHIR significantly increased collective cell anisotropic stress in spheroids at 48 hr, while Y-27632 and blebbistatin significantly decreased it (**Fig. 6D,E**). The tension increase caused by CHIR was ablated to below that of untreated control spheroids and within the physiological range of E17 mouse kidney niches by Y-27632, but not blebbistatin. Spheroids were then analyzed by immunofluorescence for the nephron progenitor marker SIX2 and the pre-tubular aggregate/renal vesicle (early nephron) marker LHX1 (**Fig. 6F,G**). We found that Y-27632 increased cell conversion to and/or self-renewal of SIX2+ progenitors (as previously reported for mouse metanephric mesenchyme cultures[79]). However, Y-27632 did not by itself induce LHX1+ cells. CHIR increased differentiation to the LHX1+ state as previously described[71], and combining CHIR with Y-27632 or blebbistatin had a strongly synergistic effect. These LHX1+ cells clustered and began to express the later medial nephron marker Jag1, indicating appropriate progression of differentiation after perturbation (**Fig. 6F**). These data together show that Wnt-driven nephron progenitor commitment is higher in a collective cell microenvironment with lower mechanical tension.

We next considered candidate signaling pathways involved in nephron progenitor commitment that are known to be mechanosensitive in other contexts. We focused our attention on quantifying pSMAD1/5 in mouse E17 tip domains due to its proposed mechanosensitive properties and role in BMP7-mediated transition of CITED1+ SIX2+ nephron progenitors to a CITED1- SIX2+ state 'primed' for further induction via Wnt/β-catenin[14,56,80]. We observed that pSMAD1/5 appeared to be enriched in cap mesenchyme cells within recently branched tip domains since mean pSMAD1/5 levels in caps positively correlated with the shape index of their tip domains, but not their area (**Fig. 6H, Fig. S7**). These data show that SMAD signaling relevant to progenitor priming is spatiotemporally correlated with tip life-cycle, making it a second candidate for cell integration of geometric and/or mechanical cues with nephrogenic decision making.

## Discussion

Gaining a fundamental understanding of tissue-wide coordination between ureteric bud epithelial and nephron morphogenesis would lead to more precise control strategies for addressing variability in nephron endowment between kidneys[81–83]. However, nephron number is set by complex signaling interactions within and between cell populations local to UB tips. Perturbing levels of key factors including Six2[84] and Tsc1[81] can have paradoxical effects on nephrogenesis. Similarly, the same pathway can regulate both nephron progenitor renewal and differentiation at different levels or in closely related cell states (Wnt/β-catenin[85,86]) or through

different downstream effectors (BMP/MAPK vs. BMP/SMAD[82]). Kidney organoids constitute both a promising platform to clarify the fundamentals of nephrogenesis and a vehicle toward augmentation of adult kidney function. However, nephrons form in a single synchronous pulse in iPSC-derived kidney organoids rather than in an ongoing, periodic manner[12,87]. Replicating the latter in organoids is a significant opportunity since successive rounds of nephrogenesis is crucial to achieving high nephron density in *vivo*.

Despite evidence of tight control over nephron progenitor differentiation at the signaling level, an overarching pace-maker that explains the consistent number ratio of nephrons to UB tips seen over E15-P2[17] has not been described. Progenitors stochastically enter and exit concave UB tubule 'armpit' regions that might concentrate secreted inductive factors, but no such shape-dependence has been found[25,85]. We decided instead to characterize the geometric reference frame of tip domains over an inferred life-cycle to uncover other possibilities. Our results suggest that topological requirements imposed by decreasing curvature of the kidney and closer packing of tip domains forces them into semi-crystalline organization after ~E15 (**Fig. 7A**). Two bodies of theory predict density-dependent and -independent contributions to a rigidity transition in tip domains that coincide with this. We note that flattening of the kidney surface as it grows could also reinforce this by increasing the critical shape index at which rigidification occurs[88]. The predicted rigidity transition coincides with an increase in solid-like properties at the kidney surface, creating the potential for residual stresses to exist. Physical resistance to tip duplication as they displace jammed neighbors would mean that each tip domain experiences temporal waves in mechanical stress (**Fig. 7B**). Indeed, we find that mechanical stresses local to tip domains correlate with their life-cycle at E17 but not prior to the rigidity transition at ~E15.

Could cyclical mechanical stress in the niche serve as a pace-making signal that then synchronizes nephron formation with UB branching? The compositional and dynamic complexity of kidney morphogenesis drove us to reductionist perturbations of cell collective tension in nephron progenitor spheroids, which model early nephrogenesis[14,71,72]. Perturbing collective cell contractility to model the lower stress nephrogenic microenvironment later in the tip domain life-cycle increased nephrogenesis in this *in vitro* system. Although we do not pinpoint the mechanotransduction pathways involved, our organoid and explant data suggest further investigation of mechanical modulation of BMP/pSMAD and Wnt9b/β-catenin pathways (and the potential for synergy between them, **Note S7**). Our data fit a hypothesis previously applied to the cessation of nephrogenesis, where increasing BMP7/SMAD signaling at the expense of BMP7/MAPK is predicted to increase differentiation of nephron progenitors at the expense of self-renewal by sensitizing them to Wnt/β-catenin mediated differentiation as development progresses[14,82,89]. However, we apply a similar logic on the timescale of tip duplication (**Fig. 7B**). In this narrative, a pulse of mechanical stress at the beginning of each tip duplication cycle increases BMP7/pSMAD activity in analogy to its role in digit formation[56]. This would prime an appropriate fraction of nephron progenitors for Wnt-induced commitment later in the tip duplication life-cycle when mechanical stress decreases in the niche. Alternating periods of high and low stress may then constitute a pace-maker for nephron formation.

Other hypotheses are partially consistent with the data since niche geometry and mechanics are correlated. For example, a high tip domain shape index shortly after branching could increase contact surface area of FOXD1+ FAT4+ stroma with nephron progenitors, which are known to promote their differentiation[90–92]. We decoupled geometry and mechanics using a reductionist organoid system where the data argue against this interpretation, but future work is warranted. In any case, a mechanical perspective on nephrogenesis here led us to a 4.5-to-22-fold increase in early nephron formation in iPSC-derived organoid models relevant to regenerative medicine.

A broader understanding of connections between kidney geometry, mechanics, and niche signaling holds significant promise for exerting engineering control over the time and place of nephron formation in regenerative medicine applications. Future work will investigate if biochemical perturbation of nephron progenitor mechanics can be phenocopied with other control strategies, including cyclical application of external mechanical stress, or optogenetic perturbation of tension in nephron progenitors or stroma. Additional studies will also be necessary to determine how geometric and mechanical cues shape biochemical cross-talk between ureteric bud tip, cap mesenchyme and stromal progenitor cell populations. These efforts will contribute to an exciting opportunity to gain engineering control over periodic and ongoing nephron formation in next-generation kidney organoids.

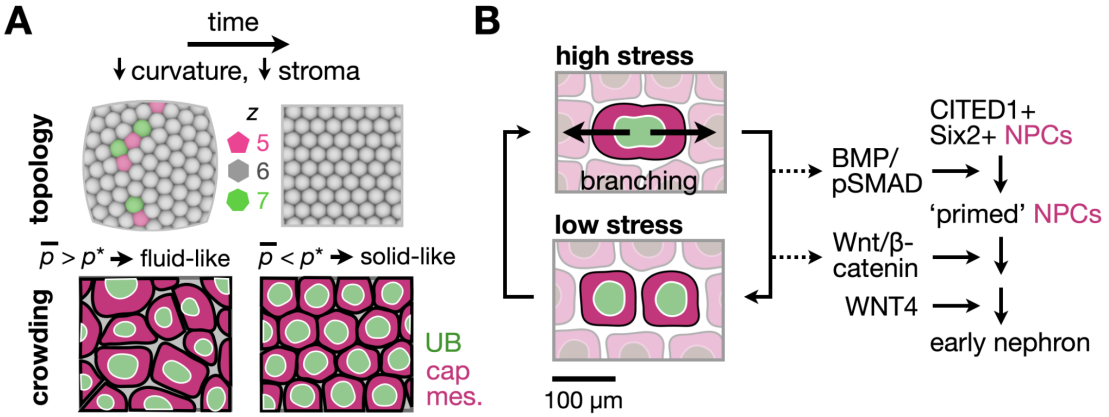


**Fig. 7: Model for curvature and crowding contributions to tip domain packing and its effects on mechanics and differentiation in the nephrogenic niche.** (**A**) Schematic summary of curvature and crowding contributions to tip domain geometry and rigidity transition. (**B**) Schematic summary of cyclical mechanical stress in the tip domain microenvironment associated with tip duplication life-cycle, and hypothesis for mechanical licensing of differentiation signaling in nephron progenitors (NPCs).


**Acknowledgements**

We would like to thank Hughes lab members, Zev Gartner, Celeste Nelson, and Melissa Little for discussion and advice. We are grateful to Kate Bennett at the Molecular Pathology and Imaging Core, Gastroenterology Division, Penn Medicine for technical assistance with laser ablation studies; Wenli Yang at the iPSC Core Facility, Division of Translational Medicine and Human Genetics, Penn Medicine and Ananya Gupta for assistance with iPSC protocols; David Li and Paul Janmey for access to and training on microindentation; and Nate Petrikas for assistance with qPCR. This work was supported by: NIH F32 fellowship DK126385 (LSP), the Predoctoral Training Program in Developmental Biology T32HD083185 (JMV), NSF GRFP (CMP), NIH NIGMS MIRA R35GM133380 (AJH), NIH NIDDK R01DK132296 (AJH), NSF CAREER award 2047271 (AJH).


**Author contributions**

Conceptualization: JMV, LSP, TJC, AJH
Methodology: JMV, LSP, JL, AH, TJC, GHL, CMP, JZ, AJH
Software: JMV, TJC, JZ, AJH
Formal analysis: JMV, TJC, JZ, AJH
Investigation: JMV, LSP, JL, AH, TJC, GHL, CMP, CS, JZ, AJH
Writing - original draft: JZ, AJH
Writing - review and editing: JMV, LSP, JL, AH, TJC, GHL, CMP, JZ, AJH
Visualization: JMV, LSP, TJC, GHL, CS, JZ, AJH
Supervision: LSP, JZ, AJH
Project administration: JZ, AJH

**Declaration of interests**

Authors declare that they have no competing interests.

**Data and materials availability**

All data necessary to evaluate conclusions of this study are presented in the paper and supplementary materials. In-house code and raw data are available from the authors upon request.

## Methods

**Animal experiments.** Mouse protocols followed NIH guidelines and were approved by the Institutional Animal Care and Use Committee of the University of Pennsylvania. E14-E17 embryos were collected from timed pregnant CD-1 mice (Charles River) and stages confirmed by limb anatomy as previously described[93]. Embryonic kidneys were dissected in chilled Dulbecco's phosphate buffered saline (DPBS, MT21-31- CV, Corning)[94].

**Kidney immunofluorescence imaging.** Immunofluorescence staining and imaging was performed as previously described[18], using protocols adapted from Combes *et al.* and O'Brien *et al.*[95,96]. Briefly, dissected kidneys were fixed in ice cold 4% paraformaldehyde in DPBS for 20 min, washed three times for 5 min per wash in ice cold DPBS, blocked for 2 hr at room temperature in PBSTX (DPBS + 0.1% Triton X- 100) containing 5% donkey serum (D9663, Sigma), incubated in primary and then secondary antibodies in blocking buffer for at least 48 hr at 4$^{o}$C, alternating with 3 washes in PBSTX totaling 12-24 hours. The minimum duration of primary and secondary incubations and washes depended on the age of the kidney, as previously described[95].

Primary antibodies and dilutions included rabbit anti-Six2 (1:600, 11562-1-AP, Proteintech, RRID: AB_2189084), mouse anti-E-cadherin (1:200, clone 34, 610404, BD Biosciences, RRID: AB_397787), rat anti-E-cadherin (1:100, ab11512, abcam, RRID:AB_298118), rabbit anti-phospho-Smad1/5 (1:800, 9516, Cell Signaling Technology, RRID:AB_491015), mouse anti-calbindin D-28K (1:100, clone CB-955, C9849, Sigma, RRID: AB_476894), mouse anti-pan-cytokeratin (1:200, clone 11, C2931, Sigma, RRID:AB_258824), and goat anti-jagged 1 (1:150, AF599, R&D Systems, RRID: AB_2128257). Secondary antibodies (all raised in donkey) were used at 1:300 dilution and include anti-rabbit AlexaFluor 647 (A31573, ThermoFisher, RRID: AB_2536183), anti-rabbit AlexaFluor 555 (A31570, ThermoFisher, RRID: AB_2536180), anti-mouse AlexaFluor 555 (A31572, ThermoFisher, RRID: AB_162543), anti-goat AlexaFluor 488 (A11055, ThermoFisher, RRID: AB_2534102), anti-rat AlexaFluor Plus 555 (A48270, ThermoFisher, RRID: AB_2896336), anti-rabbit AlexaFluor 488 (A21206, ThermoFisher, RRID: AB_2535792), and anti-rat AlexaFluor Plus 405 (A48268, ThermoFisher, RRID: AB_2890549). In some experiments, samples were counterstained in 300 nM DAPI (4',6-diamidino-2-phenylindole; D1306, ThermoFisher), 20 µg ml$^{-1}$ AlexaFluor 488-labeled peanut (*Arachis hypogaea*) agglutinin lectin (PNA, L21409, Sigma), and/or 1:40 AlexaFluor 647 phalloidin (A22287, ThermoFisher) diluted in blocking buffer for 2 hours at room temperature, followed by 3 washes in PBS.

Kidneys were imaged in wells created with a 2 mm diameter biopsy punch in a ~5 mm-thick layer of 15:1 (base:crosslinker) polydimethylsiloxane (PDMS) elastomer (Sylgard 184, 2065622, Ellsworth Adhesives) set in 35 mm coverslip-bottom dishes (FD35-100, World Precision Instruments). Imaging was performed using a Nikon Ti2-E microscope equipped with a CSU-W1 spinning disk (Yokogawa), a white light LED, laser illumination (100 mW 405, 488, and 561 nm lasers and a 75 mW 640 nm laser), a Prime 95B back-illuminated sCMOS camera (Photometrics), motorized stage, 4x/0.2 NA, 10x/0.25 NA and 20x/0.5 NA lenses (Nikon), and a stagetop environmental enclosure (OkoLabs).

**Human iPSC-derived nephron progenitors.** Nephron progenitor cells were generated from SIX2$^{EGFP}$ transgenic reporter iPSC line (*SIX2*-T2A-*EGFP*, Murdoch Children's Research Institute / Kidney Translational Research Center, Washington University Nephrology)[97] according to published protocols[76]. Briefly, iPSCs were maintained in standard tissue-culture treated 24-well plates in stem cell maintenance medium plus supplement (mTeSR+ kit, StemCell Technologies 100-0276) and 1x Penn/Strep from a 100x stock (Mediatech, MT30-002-

Cl). Cells were passaged using Accutase (StemCell Technologies, 07920) and plated at a density of 25,000 cells per well. Differentiation was induced with Advanced RPMI 1640 Medium (Fisher Scientific, 12-633-012), GlutaMAX (ThermoFisher, 35050061), 1x Penn/Strep and 7μM CHIR 99021 (Tocris, 4423) either the next day or when cells reached 50-75% confluency. On day 4, media was changed to Advanced RPMI 1640 Medium, Glutamax, 1x Penn/Strep and 10 ng $ml^{-1}$ activin (R&D Systems, 338AC010CF). On Day 7 media was changed to Advanced RPMI 1640 Medium, Glutamax, 1x Penn/Strep and 10 ng $ml^{-1}$ FGF9 (R&D Systems, 273-F9-025). On day 9 (metanephric mesenchyme stage), cells were either 1) differentiated further in 10 ng $ml^{-1}$ FGF9 until day 21 with a 3 μM CHIR pulse over days 9-11, 2) dissociated and aggregated for use in spheroid experiments, or 3) cultured for up to 3 days in 10 ng $ml^{-1}$ FGF9 media to maintain them in the SIX2+ state.

**2D iPSC-derived nephron progenitor immunofluorescence microscopy.** Nephron progenitor cell 2D cultures were fixed in ice-cold 4% paraformaldehyde for 10 minutes. Fixed cells were then washed 2X in PBSG (DPBS + 7.5 g/L glycine) 5 minutes each then washed once in DPBS. Cells were then permeabilized in 0.5% Triton-X-100 for 5 minutes at 4C. Then cells were blocked for 1hr at room temperature in IF Wash (DPBS + 1g/L Bovine Serum Albumin + 0.2% Triton-X-100 + 0.04% Tween-20) + 10% donkey serum. Cells were then incubated overnight at 4C in appropriate dilution of primary antibody in IF Wash + 10% donkey Serum. Cells were then washed 3X in IF wash at room temperature totaling 30 minutes then incubated in appropriate dilution of secondary antibody at room temperature in IF wash + 10% donkey serum. Cells were again washed 3X in IF wash totaling 30 minutes. Samples were counterstained in 300 nM DAPI in DPBS and washed 1X in DPBS then imaged using confocal microscopy. Primary antibodies and dilutions included mouse anti-E-cadherin (clone 34, 1:200, 610404, BD Biosciences, RRID: AB_397787), rabbit anti-SLC12A1 (1:300, ab171747, Abcam, RRID: AB_2802126), goat anti-Gata3 (1:20, AF2605, R&D Systems, RRID: AB_2108571). Secondary antibodies (all raised in donkey) were used at 1:300 dilution and include anti-rabbit AlexaFluor 647 (A31573, ThermoFisher, RRID: AB_2536183), anti-goat AlexaFluor 488 (A11055, ThermoFisher, RRID: AB_2534102), and anti-mouse AlexaFluor 555 (A31572, ThermoFisher, RRID: AB_162543).

**Validation of iPSC differentiation by qPCR.** RNA extraction was performed on cells from individual wells of a 24-well tissue-culture dish at each differentiation time-point using an RNEasy mini kit (Qiagen 74104). cDNA was generated from RNA using an Applied Biosystems High Capacity cDNA Reverse Transcription kit (ThermoFisher 4368814), following the manufacturer protocol and using 2 ng of RNA in the reaction for each sample. Applied Biosystems Sybr Green PCR Master Mix (ThermoFisher 4344463) was used for qPCR in an Applied Biosystems 7300 thermocycler. Applied Biosystems suggested protocol for Sybr Green PCR Master Mix was followed for temperatures and times. 25 ng of cDNA were used in each reaction along with the appropriate qPCR primers at 300 nM. qPCR primers for *ACTB*, *OSR1*, and *PAX2* were used as previously described[71]. DeltaDeltaCt values were calculated using *ACTB* as a housekeeping gene.

**Nephron progenitor spheroid differentiation assays.** Day 9 cap mesenchyme-stage nephron progenitors were lifted with Accutase and re-plated at 50,000 cells per well in 96-well ultra low attachment round-bottom plates (Corning 7007) in Advanced RPMI 1640 Medium, Glutamax, 1x Penn/Strep and 10 ng $ml^{-1}$ FGF9 ("basal media") plus the specified perturbation conditions, which included 3 μM CHIR, 10 μM Y27632 (StemCell Technologies, 72304) from a 10 mM stock in DMSO, and/or 30 μM (S)-(-)-blebbistatin (Tocris, 1852) from a 30 mM stock in DMSO. Cells were then aggregated by plate centrifugation at 300 g for 30 s. After 48 hr in culture, spheroids were collected and transferred to 1.7mL tubes using a p200 pipette tip widened by cutting the tip to size with a razor blade. Excess media was removed and spheroids were fixed in ice-cold 4% paraformaldehyde in PBS for 15 min. Spheroids were then stained for immunofluorescence microscopy similar to kidneys (see **Kidney immunofluorescence imaging.**) via primary and secondary antibody incubation for 48 hr each at 4C and washes in PBSTX totaling 6 hours. Primary antibodies and dilutions included mouse anti-

Lhx1 (1:50, 4F2, Developmental Studies Hybridoma Bank, University of Iowa, RRID: AB_531784) and rabbit anti-Six2 (1:600, 11562-1-AP, Proteintech, RRID: AB_2189084). Spheroids were then incubated in 1 µg $ml^{-1}$ DAPI in PBS at 4C for 1hr before washing once in ice-cold PBS. Spheroids were transferred for imaging using a widened p200 pipette tip to a cover-slip bottom 24-well plate (Greiner 662892). Excess PBS was removed and spheroids were incubated with ~20 µl of FocusClear (Cedarlane Labs, FC-101) for 20 min at room temperature prior to confocal imaging. Spheroids were imaged using 5 µm z-steps.

**Quantification of spheroid cell differentiation.** Maximum intensity projections of spheroids were generated and further processed in FIJI. DAPI signal was used to segment spheroids and calculate their areas in number of pixels. SIX2 and LHX1 signal was segmented using 50 pix rolling ball background subtraction and thresholding to remove background signal. The total numbers of SIX2+ and LHX1+ pixels were then divided by the total number of DAPI+ pixels to normalize positive pixels by spheroid area.

**Embryonic kidney data annotation.** UB tip positions were manually annotated from confocal stacks in FIJI using the *multi-point* tool. Nephrons per tip were manually annotated from confocal stacks of the SIX2 and PNA channels, summing across SIX2+ pre-tubular aggregates/early renal vesicles and later stages for which connecting tubule junctions with UB tips were visible as circular intersections in the PNA channel at tips.

Confocal immunofluorescence stacks on the SIX2 channel were manually annotated to extract kidney outlines at each *z* plane by manually tracing in FIJI on an Apple iPad. These outlines constituted a binary mask stack used for input to curvature analysis.

**Voronoi, shape index, and defect charge analysis.** Delaunay triangulations and Voronoi diagrams were created from UB tip coordinates in MATLAB, roughly filtered by polygon area and manually edited to remove edge cells. The coordination number was determined as the number of sides of each Voronoi cell, and shape index $p$ was determined via $p = P/\sqrt{A}$, where $P$ is the perimeter of a Voronoi cell and $A$ is its area. Heat maps of shape index were produced by interpolation of shape index data in MATLAB using the 'v4' method in griddata.m. The total disclination defect charge $Q$ for a particular Voronoi diagram was determined by summing the topological charges $s$ over all Voronoi cells (note: $s = 6 - z$, where $z$ is the coordination number of a cell).

**Packing model.** We used physics-based modeling in the Rhino (v7, Robert McNeel & Associates) Grasshopper Kangaroo2 environment (Daniel Piker) to demonstrate repulsive sphere packing on flat surfaces and spheres in **Fig. 1B** and a kidney surface mesh in **Movie S2** (see **Kidney curvature analysis**). Quantitative principles of this software environment are detailed in ref. [18]. We used the *SphereCollide* goal to model sphere mutual repulsion and the *OnMesh* goal to hold spheres at flat or curved interfaces, each with arbitrarily high energy potential weightings to mimic previously described features of particle packings on surfaces[19–21,98]. To create overlay schematics, sphere coordinates were exported from Rhino and used as input to the same Voronoi and coordination number analysis performed in MATLAB.

**Kidney curvature analysis.** 3D mask stacks of kidney outlines were first exported from 3D viewer in FIJI as binary .stl meshes representing kidney surfaces (**Fig. S1**). These .stl files were then imported into Rhino, remeshed down to ~1,000 polygons using quad remesh, smoothed, triangulated, draped, and split to remove the bottom face. Contour cross-sections were created at 20 µm increments along the long axis and lofted to create a smooth, regular mesh representing the outer kidney surface. Surface meshes were exported as .stl files, imported into MATLAB and represented as height maps using stlread and trisurf commands. Exported meshes were also analyzed to determine the Gaussian curvature local to each polygon via a custom workflow in Rhino Grasshopper. The area-weighted sum of polygon curvature, $I = \int_A G \, dA$ over an equivalent area

covered by the Voronoi diagram for that surface was then used to compute the integrated Gaussian curvature in units of disclinations, $\Omega = \frac{I}{\pi/3}$.

**Rigidity analysis.** We describe close-packed tip domains using a 2D cell vertex model[42,44,99,100], representing the mechanical energy of each tip domain by:

$$E_i = K(A_i - A_0)^2 + \xi P_i^2 + \gamma P_i$$

Where the first term represents collective cell elasticity (stiffness) in tip domains, a product of a stiffness constant and actual and preferred domain cross-sectional areas respectively. The second term represents collective cell contractility in tip domains, a product of a constant and the square of the cell perimeter, and the third term represents an interfacial line tension proportional to cell perimeter, set by competition between stroma contractility and cell-cell adhesion at the cap mesenchyme-stroma boundary (**Fig. 5A**). These terms are analogous to cell elasticity, cortical contractility, and interfacial tension terms for confluent monolayers. These energy terms are justified firstly by macroscopic behavior of embryonic kidney cortex explants, which actively contract and round up without loss of tip domain adhesion to neighbors in the hours after cutting[18]. Secondly, elasticity of tip domains is implied by positive stiffness values returned by microindentation on a length-scale appropriate to tip domain extents in *xy* and *z* (**Fig. 3F**), and interfacial line tensions are implied by rebound velocities being positive in domain-domain interface ablation experiments (**Fig. 5F**).

Several lines of analysis predict a rigidity transition in cell/uncoupled tip domain systems governed by the above energy equation at a critical shape index of $p^* = 3.81$, the simplest of which is isostaticity (degree of freedom analysis)[42]. Bi *et al.* began from Euler's formula for polygons tiling the 2D plane with periodic boundary conditions: 0 = V - E + M, where E is the number of edges, V is the number of vertices, and M is the number of cells[42]. Since two cells share each edge, Mz = 2E, where z is the coordination number. These two expressions give V = M(z/2 - 1). The degrees of freedom $n_{dof} = 2V$ account for translation of each vertex in 2D. Three constraints per cell are needed for rigidity (to achieve a force balance constraining 2D translation and a torque balance constraining rotation), i.e. $n_c = 3M$. At isostaticity (rigidity), $n_{dof} = n_c$, i.e. 2V = 3M. Substituting into Euler's formula then gives $z_{iso} = 5$. This suggests that rigidity will occur when the median shape index drops below the shape index of a pentagon = $p^* \simeq 3.81$.

However, for coupled tip domains in which daughter tubules share a physical linkage through their parent node, we note that only two constraints rather than three are needed for one of each couple, since one translational constraint is accounted for by the physical linkage. This makes $n_c = 2.5M$ and at isostaticity, 4V = 5M, giving $z_{iso} = 4.5$. Rigidity should therefore occur when the median shape index drops below that for an equal mixture of squares and pentagons, implying $p^* = (4+3.81)/2 \simeq 3.91$.

**Spatial autocorrelation analysis.** 2D spatial autocorrelation heatmaps of tip regions were computed from maximum projections of confocal *z* stacks on the PNA fluorescence channel using the Wiener-Khintchine theorem in MATLAB (autocorr2d.m, Tristan Ursell).

**Brillouin microscopy.** A confocal Brillouin microscope was used for acquiring mechanical images of kidneys. A detailed description of the instrumentation is published in a previous report[101]. Briefly, the Brillouin microscope consisted of a Brillouin spectrometer and a commercial fluorescence microscope (IX83, Olympus). A continuous wave laser (~17 mW, 660 nm, Torus, Laser Quantum) was used as light source. The laser beam was focused into a spot of 0.7 μm x 0.7 μm x 2 μm using a 40x/0.6 objective lens (Olympus). The high-

resolution Brillouin spectrometer was built from a two-stage virtually imaged phased array (FSR = 15 GHz, LightMachinery). The spectrometer is shot-noise limited and has a spectral precision of 0.01 GHz, suggesting a sensitivity of 0.16% for water-based materials. The Brillouin spectra were collected using an EMCCD camera (iXon life 897, Andor). During the Brillouin experiment, kidney tip domains were scanned at room temperature with a step size of 1 μm and an acquisition speed of 50 ms per point. UB tip PNA fluorescence was also imaged on a separate channel to later register with the corresponding Brillouin images.The longitudinal modulus ($M'$) is determined by the measured Brillouin shift ($v_B$) via the relationship $M' = v_B^2 \bullet \lambda^2 \cdot \rho \ / \ 4n^2$, where $\lambda$ is the wavelength of the laser, $n$ and $\rho$ are the refractive index and density of the sample, respectively. To calculate the longitudinal modulus, we estimated $n = 1.40$ from literature measurements of adult kidney[102]. The density was calculated as 1.096 g/ml based on a published relationship between refractive index and density for biological materials[48]. According to the linear log-log relationship between longitudinal modulus ($M'$) and Young's modulus (*E*), the relative changes of both moduli are related by $\Delta E/E = (1/a) \cdot \Delta M/M$, where the coefficient $a = 0.0617$ was obtained by calibration with an atomic force microscope using NIH 3T3 cells[51].

**Microindentation.** Free-standing explanted mouse kidneys were micro-indented using established methods[53]. Instrumentation was the same as described by Levental *et al.*, except indenter arm height was controlled by a stepper motor (L4018S1204-M6, Nanotec, Munich) rather than a hydraulic micromanipulator. The indenter was fabricated from cylindrical 30 gauge (AWG) SAE 316L stainless steel wire having a diameter of 255 μm. Briefly, after calibrating the spring constant of the tensiometric sensor, each kidney was placed in a 35 mm culture dish and bulk media wicked away to leave the kidney surface semi-dry. The indenter was immediately lowered at a rate of 12.5 μm $s^{-1}$ using the z-stage of the instrument to an indentation depth of ~30 μm into the kidney surface while automatically recording time, force on the indenter, and indenter *z* position. Indentation was then halted and force vs. time recorded for an additional 60-120 s. Stiffness was inferred using the following relationship for indentation of a soft homogeneous material by a flat hard surface:

$$E_{\text{tissue}} = \frac{F_{\text{appl}}\left(1 - \nu_{\text{tissue}}^2\right)}{h_{\text{ind}}.\kappa.2r}$$

Where $F_{appl}/h_{ind}$ is the slope of force vs. indentation depth from the point of contact after accounting for sensor spring constant. $\nu$ is the Poisson ratio of the tissue, assumed to be 0.5. $\kappa$ is the Hayes correction factor[103], accounting for finite sample thickness ($\kappa$ was determined for each stage based on average kidney width inferred from confocal image stacks), and 2*r* is the diameter of the probe (255 μm).

Similar to previous analysis[53], force vs. time (*t*) traces at fixed indentation depth were normalized to maximum force and fit to the following three-parameter relaxation relationship using non-linear least-squares fitting in MATLAB:

$$F_{\text{norm}} = 1 - (1 - G_\infty)(1 - e^{-t/\tau}) - kt$$

This relationship implies a Kelvin-Voigt material with an extra viscous damper in series, where $G_\infty$ and $\tau$ are an equilibrium modulus and relaxation time constant, respectively. We refer to *k* as a viscous relaxation constant in this work.

**Force inference.** Bayesian force inference was applied according to a recently published procedure that infers maps of tissue tension and pressure based on observed variations in edge lengths and angles at cell vertices,

assuming that tissues are in instantaneous mechanical equilibrium, tissue mechanics are dominated by in-plane tensions and pressures, and that interfacial tensions are positive[59,61]. The Bayesian approach is appropriate here, since it is less reliant on accurate measurement of interface curvatures, making it ideal for cases with large numbers of cells and small interfacial curvatures[61]. Voronoi diagrams were first processed in the *Tissue Analyzer* plugin in FIJI[104], and segmentation output data were then passed to MATLAB for Bayesian force inference using code published by Kong et al.[61], which was adapted from earlier work by Ishihara et al.[59]. We used this code to compute stress tensors and their isotropic and anisotropic (deviatoric) components for each tip domain using Batchelor's formula[61]. Since stress outputs are relative here, we normalized them to the largest median stress in a given set of comparisons.

**Laser ablation.** E17 kidney explants were labeled in 20 µg $ml^{-1}$ Alexa Fluor 488-PNA and 1:1000 CellTracker Red (ThermoFisher C34552, 10 mM stock in DMSO) in Dulbecco's minimum essential medium (DMEM, 10-013-CV, Corning) for 1 hour at 37°C, washed 3x in DMEM and placed in 2mm-diameter PDMS wells (see **Kidney immunofluorescence imaging**), this time plasma bonded to a quartz coverslip (No. 1 thickness, Ted Pella, 26014) to maximize UV transmission. Kidneys were ablated using a 355 nm UV laser (Molecular Machines & Industries, SL µCut v1.0) through a 10x objective on a Nikon Ti2 controlled by MMI software. Cut opening time-lapses were imaged from the microscope monitor using an iPhone 8 video camera and spatially calibrated using on-screen fiducial marks in the MMI software. Kidneys were fixed after ablations in ice cold 4% PFA for 15 min, washed 3x with PBS and imaged by confocal microscopy (see **Kidney immunofluorescence imaging**).

**scRNA-seq analysis.** Gene expression matrices generated from scRNA-seq of dissociated E15.5 mouse embryonic kidneys in Lawlor *et al.* were used[25]. These matrices were accessed from the Gene Expression Omnibus (GEO, NCBI) under accession code GSE118486 and sample mk1 was used for further analysis. Analysis was done similarly to Lawlor *et al.* In short, the Seurat library[105,106] was used to import the gene expression matrix to R and for downstream analyses. Cells with less than 200 genes expressed or with greater than 7.5% mitochondrial gene expression were removed. Genes expressed in less than 3 cells were removed from the dataset. The filtered dataset contained 2,708 cells with an average of 2,441 unique genes detected per cell. Cell cycle scoring was done using the CellCycleScoring function. Scaled data matrices were then generated using the ScaleData function. Shared nearest neighbor (SNN) clustering was performed for whole kidney data using resolution 0.5 for the first 15 principal components calculated from a set of 2000 variable genes. Differentially expressed marker genes were identified using a Wilcoxon rank sum test and compared to the published list of marker genes from Lawlor *et al.*[25] to assign cell identity. SNN clustering was then performed on cells belonging to the nephron lineage clusters using resolution 0.5 for the first 12 principal components calculated from a set of 2000 variable genes. Again, differentially expressed marker genes were identified in Seurat using Wilcoxon rank sum test and compared to a list of marker genes for distinct nephron lineage clusters published by Lawlor *et al.*[25] to assign cell identity. Fold-change and Wilcoxon rank sum *p*-value for individual genes in volcano plots were calculated by comparing the committing cluster to the progenitor cell clusters.

**Gene Set Enrichment Analysis (GSEA).** An unranked list of 171 highly upregulated genes in the committing cluster compared to the progenitor cell cluster was generated by taking genes with $\log_2$(fold-change) of at least 0.25 and Bonferroni corrected adjusted Wilcoxon rank sum test *p*-value less than 0.05 between the clusters. The top 10 most statistically significant overrepresented Gene Ontology terms in this gene set were found using the Gene Set Enrichment Analysis (GSEA) online software[107], to compare this gene list to Gene Ontology (GO) gene sets[68]. Gene set enrichment plots were generated using GSEA desktop software. All genes expressed in at least 3 cells were ranked using $\log_2$(fold-change) of average expression in the

committing cluster against the progenitor clusters in Lawlor *et al.*[25] to compare against the specified gene sets[25].

**Statistical analysis.** One-way analysis of variance (ANOVA) with correction for multiple comparisons using Tukey's honestly significant difference test was performed in MATLAB using anova1.m and multcompare.m functions.

## References


1. Rumballe, B. A. *et al.* Nephron formation adopts a novel spatial topology at cessation of nephrogenesis. *Dev. Biol.* **360**, 110–122 (2011).
2. Pohl, M., Bhatnagar, V., Mendoza, S. A. & Nigam, S. K. Toward an etiological classification of developmental disorders of the kidney and upper urinary tract. *Kidney Int.* **61**, 10–19 (2002).
3. Brenner, B. M. & Mackenzie, H. S. Nephron mass as a risk factor for progression of renal disease. *Kidney Int. Suppl.* **63**, S124-7 (1997).
4. Brenner, B. M., Garcia, D. L. & Anderson, S. Glomeruli and blood pressure. Less of one, more the other? *Am. J. Hypertens.* **1**, 335–347 (1988).
5. Osathanondh, V. & Potter, E. L. DEVELOPMENT OF HUMAN KIDNEY AS SHOWN BY MICRODISSECTION. II. RENAL PELVIS, CALYCES, AND PAPILLAE. *Arch. Pathol.* **76**, 277–289 (1963).
6. Lefevre, J. G. *et al.* Branching morphogenesis in the developing kidney is governed by rules that pattern the ureteric tree. *Development* **144**, 4377–4385 (2017).
7. Carroll, T. J., Park, J.-S., Hayashi, S., Majumdar, A. & McMahon, A. P. Wnt9b plays a central role in the regulation of mesenchymal to epithelial transitions underlying organogenesis of the mammalian urogenital system. *Dev. Cell* **9**, 283–292 (2005).
8. Lu, B. C. *et al.* Etv4 and Etv5 are required downstream of GDNF and Ret for kidney branching morphogenesis. *Nat. Genet.* **41**, 1295–1302 (2009).
9. Costantini, F. & Kopan, R. Patterning a complex organ: branching morphogenesis and nephron segmentation in kidney development. *Dev. Cell* **18**, 698–712 (2010).
10. Schuchardt, A., D'Agati, V., Larsson-Blomberg, L., Costantini, F. & Pachnis, V. Defects in the kidney and enteric nervous system of mice lacking the tyrosine kinase receptor Ret. *Nature* **367**, 380–383 (1994).
11. Pichel, J. G. *et al.* Defects in enteric innervation and kidney development in mice lacking GDNF. *Nature* **382**, 73–76 (1996).
12. Little, M. H. Returning to kidney development to deliver synthetic kidneys. *Dev. Biol.* **474**, 22–36 (2021).
13. Lindström, N. O. *et al.* Integrated β-catenin, BMP, PTEN, and Notch signalling patterns the nephron. *Elife* **3**, e04000 (2015).
14. Brown, A. C. *et al.* Role for compartmentalization in nephron progenitor differentiation. *Proc. Natl. Acad. Sci. U. S. A.* **110**, 4640–4645 (2013).
15. Georgas, K. *et al.* Analysis of early nephron patterning reveals a role for distal RV proliferation in fusion to the ureteric tip via a cap mesenchyme-derived connecting segment. *Dev. Biol.* **332**, 273–286 (2009).
16. Kao, R. M., Vasilyev, A., Miyawaki, A., Drummond, I. A. & McMahon, A. P. Invasion of distal nephron precursors associates with tubular interconnection during nephrogenesis. *J. Am. Soc. Nephrol.* **23**, 1682–1690 (2012).
17. Short, K. M. *et al.* Global quantification of tissue dynamics in the developing mouse kidney. *Dev. Cell* **29**, 188–202 (2014).
18. Prahl, L. S., Viola, J. M., Liu, J. & Hughes, A. J. The developing kidney actively negotiates geometric packing conflicts to avoid defects. *bioRxiv* 2021.11.29.470441 (2021) doi:10.1101/2021.11.29.470441.
19. Irvine, W. T. M., Vitelli, V. & Chaikin, P. M. Pleats in crystals on curved surfaces. *Nature* **468**, 947–951 (2010).
20. Bausch, A. R. *et al.* Grain Boundary Scars and Spherical Crystallography. *Science* **299**, (2003).
21. Jiménez, F. L., Stoop, N., Lagrange, R., Dunkel, J. & Reis, P. M. Curvature-Controlled Defect Localization in Elastic Surface Crystals. *Phys. Rev. Lett.* **116**, 104301 (2016).
22. Brojan, M., Terwagne, D., Lagrange, R. & Reis, P. M. Wrinkling crystallography on spherical surfaces. *Proc. Natl. Acad. Sci. U. S. A.* **112**, 14–19 (2015).
23. Bowick, M. J. & Giomi, L. Two-dimensional matter: order, curvature and defects. *Adv. Phys.* **58**, 449–563 (2009).
24. Combes, A. N., Lefevre, J. G., Wilson, S., Hamilton, N. A. & Little, M. H. Cap mesenchyme cell swarming during kidney development is influenced by attraction, repulsion, and adhesion to the ureteric tip. *Dev. Biol.* **418**, 297–306 (2016).
25. Lawlor, K. T. *et al.* Nephron progenitor commitment is a stochastic process influenced by cell

migration. *Elife* **8**, (2019).
26. Wilson, S. B. & Little, M. H. The origin and role of the renal stroma. *Development* **148**, (2021).
27. Davies, J. A., Hohenstein, P., Chang, C.-H. & Berry, R. A self-avoidance mechanism in patterning of the urinary collecting duct tree. *BMC Dev. Biol.* **14**, 35 (2014).
28. England, A. R. *et al.* Identification and characterization of cellular heterogeneity within the developing renal interstitium. *Development* **147**, (2020).
29. Yao, Z. Stress-induced ordering of two-dimensional packings of elastic spheres. *Phys Rev E* **101**, 062904 (2020).
30. Liu, A. J. & Nagel, S. R. The Jamming Transition and the Marginally Jammed Solid. *Annu. Rev. Condens. Matter Phys.* **1**, 347–369 (2010).
31. Sullivan, J. M. The Geometry of Bubbles and Foams. in *Foams and Emulsions* (eds. Sadoc, J. F. & Rivier, N.) 379–402 (Springer Netherlands, 1999).
32. Honda, H. Description of cellular patterns by Dirichlet domains: the two-dimensional case. *J. Theor. Biol.* **72**, 523–543 (1978).
33. Munro, D. A. D., Hohenstein, P. & Davies, J. A. Cycles of vascular plexus formation within the nephrogenic zone of the developing mouse kidney. *Sci. Rep.* **7**, 3273 (2017).
34. Princen, H. M. Rheology of foams and highly concentrated emulsions. II. experimental study of the yield stress and wall effects for concentrated oil-in-water emulsions. *J. Colloid Interface Sci.* **105**, 150–171 (1985).
35. Princen, H. M. Rheology of foams and highly concentrated emulsions: I. Elastic properties and yield stress of a cylindrical model system. *J. Colloid Interface Sci.* **91**, 160–175 (1983).
36. Cohen-Addad, S., Höhler, R. & Pitois, O. Flow in Foams and Flowing Foams. *Annu. Rev. Fluid Mech.* **45**, 241–267 (2013).
37. Mason, T. G., Bibette, J. & Weitz, D. A. Yielding and flow of monodisperse emulsions. *J. Colloid Interface Sci.* **179**, 439–448 (1996).
38. Mongera, A. *et al.* A fluid-to-solid jamming transition underlies vertebrate body axis elongation. *Nature* **561**, 401–405 (2018).
39. Blumenfeld, R. Disorder Criterion and Explicit Solution for the Disc Random Packing Problem. *Phys. Rev. Lett.* **127**, 118002 (2021).
40. Bolton, F. & Weaire, D. Rigidity loss transition in a disordered 2D froth. *Phys. Rev. Lett.* **65**, 3449–3451 (1990).
41. Bi, D., Lopez, J. H., Schwarz, J. M. & Manning, M. L. Energy barriers and cell migration in densely packed tissues. *Soft Matter* **10**, 1885–1890 (2014).
42. Bi, D., Lopez, J. H., Schwarz, J. M. & Manning, M. L. A density-independent rigidity transition in biological tissues. *Nat. Phys.* **11**, 1074–1079 (2015).
43. Park, J.-A. *et al.* Unjamming and cell shape in the asthmatic airway epithelium. *Nat. Mater.* **14**, 1040–1048 (2015).
44. Farhadifar, R., Röper, J.-C., Aigouy, B., Eaton, S. & Jülicher, F. The influence of cell mechanics, cell-cell interactions, and proliferation on epithelial packing. *Curr. Biol.* **17**, 2095–2104 (2007).
45. Broedersz, C. P., Mao, X., Lubensky, T. C. & MacKintosh, F. C. Criticality and isostaticity in fibre networks. *Nat. Phys.* **7**, 983–988 (2011).
46. Scarcelli, G. & Yun, S. H. Confocal Brillouin microscopy for three-dimensional mechanical imaging. *Nat. Photonics* **2**, 39–43 (2007).
47. Scarcelli, G. *et al.* Noncontact three-dimensional mapping of intracellular hydromechanical properties by Brillouin microscopy. *Nat. Methods* **12**, 1132–1134 (2015).
48. Schlüßler, R. *et al.* Mechanical Mapping of Spinal Cord Growth and Repair in Living Zebrafish Larvae by Brillouin Imaging. *Biophys. J.* **115**, 911–923 (2018).
49. Gouveia, R. M. *et al.* Assessment of corneal substrate biomechanics and its effect on epithelial stem cell maintenance and differentiation. *Nat. Commun.* **10**, 1496 (2019).
50. Bevilacqua, C. *et al.* High-resolution line-scan Brillouin microscopy for live-imaging of mechanical properties during embryo development. *bioRxiv* 2022.04.25.489364 (2022) doi:10.1101/2022.04.25.489364.
51. Zhang, J. *et al.* Nuclear Mechanics within Intact Cells Is Regulated by Cytoskeletal Network and Internal Nanostructures. *Small* **16**, e1907688 (2020).

52. Scarcelli, G., Kim, P. & Yun, S. H. In vivo measurement of age-related stiffening in the crystalline lens by Brillouin optical microscopy. *Biophys. J.* **101**, 1539–1545 (2011).
53. Levental, I. *et al.* A simple indentation device for measuring micrometer-scale tissue stiffness. *J. Phys. Condens. Matter* **22**, 194120 (2010).
54. Muncie, J. M. *et al.* Mechanical Tension Promotes Formation of Gastrulation-like Nodes and Patterns Mesoderm Specification in Human Embryonic Stem Cells. *Dev. Cell* **55**, 679-694.e11 (2020).
55. Shyer, A. E. *et al.* Emergent cellular self-organization and mechanosensation initiate follicle pattern in the avian skin. *Science* **357**, 811–815 (2017).
56. Parada, C. *et al.* Mechanical feedback defines organizing centers to drive digit emergence. *Dev. Cell* **57**, 854-866.e6 (2022).
57. Reginensi, A. *et al.* Yap- and Cdc42-dependent nephrogenesis and morphogenesis during mouse kidney development. *PLoS Genet.* **9**, e1003380 (2013).
58. Little, M. H. & McMahon, A. P. Mammalian kidney development: principles, progress, and projections. *Cold Spring Harb. Perspect. Biol.* **4**, (2012).
59. Ishihara, S. & Sugimura, K. Bayesian inference of force dynamics during morphogenesis. *J. Theor. Biol.* **313**, 201–211 (2012).
60. Guirao, B. *et al.* Unified quantitative characterization of epithelial tissue development. *Elife* **4**, (2015).
61. Kong, W. *et al.* Experimental validation of force inference in epithelia from cell to tissue scale. *Sci. Rep.* **9**, 14647 (2019).
62. Janmey, P. A., Wells, R. G., Assoian, R. K. & McCulloch, C. A. From tissue mechanics to transcription factors. *Differentiation* **86**, 112–120 (2013).
63. Muncie, J. M. & Weaver, V. M. The Physical and Biochemical Properties of the Extracellular Matrix Regulate Cell Fate. *Curr. Top. Dev. Biol.* **130**, 1–37 (2018).
64. Hayward, M.-K., Muncie, J. M. & Weaver, V. M. Tissue mechanics in stem cell fate, development, and cancer. *Dev. Cell* **56**, 1833–1847 (2021).
65. Vining, K. H. & Mooney, D. J. Mechanical forces direct stem cell behaviour in development and regeneration. *Nat. Rev. Mol. Cell Biol.* **18**, 728–742 (2017).
66. Priya, R. *et al.* Tension heterogeneity directs form and fate to pattern the myocardial wall. *Nature* **588**, 130–134 (2020).
67. De Belly, H. *et al.* Membrane Tension Gates ERK-Mediated Regulation of Pluripotent Cell Fate. *Cell Stem Cell* **28**, 273-284.e6 (2021).
68. Ashburner, M. *et al.* Gene Ontology: tool for the unification of biology. *Nature Genetics* vol. 25 25–29 (2000).
69. Przybyla, L., Muncie, J. M. & Weaver, V. M. Mechanical Control of Epithelial-to-Mesenchymal Transitions in Development and Cancer. *Annu. Rev. Cell Dev. Biol.* **32**, 527–554 (2016).
70. Belinky, F. *et al.* PathCards: multi-source consolidation of human biological pathways. *Database* **2015**, (2015).
71. Morizane, R. *et al.* Nephron organoids derived from human pluripotent stem cells model kidney development and injury. *Nat. Biotechnol.* **33**, 1193–1200 (2015).
72. Takasato, M. *et al.* Kidney organoids from human iPS cells contain multiple lineages and model human nephrogenesis. *Nature* **526**, 564–568 (2015).
73. Combes, A. N., Zappia, L., Er, P. X., Oshlack, A. & Little, M. H. Single-cell analysis reveals congruence between kidney organoids and human fetal kidney. *Genome Med.* **11**, 3 (2019).
74. Lindström, N. O. *et al.* Conserved and Divergent Features of Mesenchymal Progenitor Cell Types within the Cortical Nephrogenic Niche of the Human and Mouse Kidney. *J. Am. Soc. Nephrol.* **29**, 806–824 (2018).
75. Wu, H. *et al.* Comparative Analysis and Refinement of Human PSC-Derived Kidney Organoid Differentiation with Single-Cell Transcriptomics. *Cell Stem Cell* **23**, 869-881.e8 (2018).
76. Morizane, R. & Bonventre, J. V. Generation of nephron progenitor cells and kidney organoids from human pluripotent stem cells. *Nat. Protoc.* **12**, 195–207 (2017).
77. Park, J.-S. *et al.* Six2 and Wnt regulate self-renewal and commitment of nephron progenitors through shared gene regulatory networks. *Dev. Cell* **23**, 637–651 (2012).
78. Park, J.-S., Valerius, M. T. & McMahon, A. P. Wnt/beta-catenin signaling regulates nephron induction during mouse kidney development. *Development* **134**, 2533–2539 (2007).

79. Tanigawa, S., Sharma, N., Hall, M. D., Nishinakamura, R. & Perantoni, A. O. Preferential Propagation of Competent SIX2+ Nephronic Progenitors by LIF/ROCKi Treatment of the Metanephric Mesenchyme. *Stem Cell Reports* **5**, 435–447 (2015).
80. Oxburgh, L. & Robertson, E. J. Dynamic regulation of Smad expression during mesenchyme to epithelium transition in the metanephric kidney. *Mech. Dev.* **112**, 207–211 (2002).
81. Volovelsky, O. *et al.* Hamartin regulates cessation of mouse nephrogenesis independently of Mtor. *Proc. Natl. Acad. Sci. U. S. A.* **115**, 5998–6003 (2018).
82. Oxburgh, L. Growth control of the kidney. *Curr. Top. Dev. Biol.* **148**, 237–263 (2022).
83. Cebrian, C., Asai, N., D'Agati, V. & Costantini, F. The number of fetal nephron progenitor cells limits ureteric branching and adult nephron endowment. *Cell Rep.* **7**, 127–137 (2014).
84. Combes, A. N. *et al.* Haploinsufficiency for the Six2 gene increases nephron progenitor proliferation promoting branching and nephron number. *Kidney Int.* **93**, 589–598 (2018).
85. Ramalingam, H. *et al.* Disparate levels of beta-catenin activity determine nephron progenitor cell fate. *Dev. Biol.* **440**, 13–21 (2018).
86. Karner, C. M. *et al.* Canonical Wnt9b signaling balances progenitor cell expansion and differentiation during kidney development. *Development* **138**, 1247–1257 (2011).
87. Howden, S. E., Vanslambrouck, J. M., Wilson, S. B., Tan, K. S. & Little, M. H. Reporter-based fate mapping in human kidney organoids confirms nephron lineage relationships and reveals synchronous nephron formation. *EMBO Rep.* **20**, (2019).
88. Sussman, D. M. Interplay of curvature and rigidity in shape-based models of confluent tissue. *Phys. Rev. Research* **2**, 023417 (2020).
89. Blank, U., Brown, A., Adams, D. C., Karolak, M. J. & Oxburgh, L. BMP7 promotes proliferation of nephron progenitor cells via a JNK-dependent mechanism. *Development* **136**, 3557–3566 (2009).
90. Das, A. *et al.* Stromal-epithelial crosstalk regulates kidney progenitor cell differentiation. *Nat. Cell Biol.* **15**, 1035–1044 (2013).
91. Fetting, J. L. *et al.* FOXD1 promotes nephron progenitor differentiation by repressing decorin in the embryonic kidney. *Development* **141**, 17–27 (2014).
92. Mao, Y., Francis-West, P. & Irvine, K. D. Fat4/Dchs1 signaling between stromal and cap mesenchyme cells influences nephrogenesis and ureteric bud branching. *Development* **142**, 2574–2585 (2015).
93. Wanek, N., Muneoka, K., Holler-Dinsmore, G., Burton, R. & Bryant, S. V. A staging system for mouse limb development. *J. Exp. Zool.* **249**, 41–49 (1989).
94. Barak, H. & Boyle, S. C. Organ culture and immunostaining of mouse embryonic kidneys. *Cold Spring Harb. Protoc.* **2011**, db.prot5558 (2011).
95. Combes, A. N. *et al.* An integrated pipeline for the multidimensional analysis of branching morphogenesis. *Nat. Protoc.* **9**, 2859–2879 (2014).
96. O'Brien, L. L. *et al.* Wnt11 directs nephron progenitor polarity and motile behavior ultimately determining nephron endowment. *Elife* **7**, (2018).
97. Vanslambrouck, J. M. *et al.* A Toolbox to Characterize Human Induced Pluripotent Stem Cell-Derived Kidney Cell Types and Organoids. *J. Am. Soc. Nephrol.* **30**, 1811–1823 (2019).
98. Negri, C., Sellerio, A. L., Zapperi, S. & Miguel, M. C. Deformation and failure of curved colloidal crystal shells. *Proc. Natl. Acad. Sci. U. S. A.* **112**, 14545–14550 (2015).
99. Fletcher, A. G., Osterfield, M., Baker, R. E. & Shvartsman, S. Y. Vertex models of epithelial morphogenesis. *Biophys. J.* **106**, 2291–2304 (2014).
100. Nagai, T. & Honda, H. A dynamic cell model for the formation of epithelial tissues. *Philos. Mag. B* **81**, 699–719 (2001).
101. Zhang, J. & Scarcelli, G. Mapping mechanical properties of biological materials via an add-on Brillouin module to confocal microscopes. *Nat. Protoc.* **16**, 1251–1275 (2021).
102. Bolin, F. P., Preuss, L. E., Taylor, R. C. & Ference, R. J. Refractive index of some mammalian tissues using a fiber optic cladding method. *Appl. Opt.* **28**, 2297–2303 (1989).
103. Hayes, W. C., Keer, L. M., Herrmann, G. & Mockros, L. F. A mathematical analysis for indentation tests of articular cartilage. *J. Biomech.* **5**, 541–551 (1972).
104. Aigouy, B., Umetsu, D. & Eaton, S. Segmentation and Quantitative Analysis of Epithelial Tissues. *Methods Mol. Biol.* **1478**, 227–239 (2016).
105. Satija, R., Farrell, J. A., Gennert, D., Schier, A. F. & Regev, A. Spatial reconstruction of single-cell

gene expression data. *Nat. Biotechnol.* **33**, 495–502 (2015).
106. Butler, A., Hoffman, P., Smibert, P., Papalexi, E. & Satija, R. Integrating single-cell transcriptomic data across different conditions, technologies, and species. *Nat. Biotechnol.* **36**, 411–420 (2018).
107. Subramanian, A. *et al.* Gene set enrichment analysis: a knowledge-based approach for interpreting genome-wide expression profiles. *Proc. Natl. Acad. Sci. U. S. A.* **102**, 15545–15550 (2005).